Light-guided actin polymerization drives directed motility in protocells

Hideaki T. Matsubayashi[1,2,3†], Shiva Razavi[1,2,4,5], T. Willow Rock[1,2], Daichi Nakajima[6], Hideki Nakamura[1,2,7,8], Daniel A. Kramer[9], Tomoaki Matsuura[10], Baoyu Chen[9], Satoshi Murata[6], Shin-ichiro M. Nomura[6], Takanari Inoue[1,2†]

1 Department of Cell Biology, School of Medicine, Johns Hopkins University, 2 Center for Cell Dynamics, Institute of Basic Biomedical Sciences, Johns Hopkins University, 3 Frontier Research Institute for Interdisciplinary Sciences, Tohoku University, 4 Department of Biomedical Engineering, School of Medicine, Johns Hopkins University, 5 Department of Biological Engineering, School of Engineering, Massachusetts Institute of Technology, 6 Department of Robotics, Graduate School of Engineering, Tohoku University, 7 Hakubi Center for Advanced Research, Kyoto University, 8 Department of Synthetic Chemistry and Biological Chemistry, School of Engineering, Kyoto University, 9 Roy J. Carver Department of Biochemistry, Biophysics and Molecular Biology, Iowa State University, 10 Earth-Life Science Institute, Institute of Science Tokyo

†Corresponding authors. Email: hideaki.matsubayashi.e1@tohoku.ac.jp, jctinoue@jhmi.edu

Abstract

Motility is a hallmark of life's dynamic processes, enabling cells to actively chase prey, repair wounds, and shape organs. Recreating these intricate behaviors using well-defined molecules remains a major challenge at the intersection of biology, physics, and molecular engineering. Although the polymerization force of the actin cytoskeleton is characterized as a primary driver of cell motility, recapitulating this process in protocellular systems has proven elusive. The difficulty lies in the daunting task of distilling key components from motile cells and integrating them into model membranes in a physiologically relevant manner. To address this, we developed a method to optically control actin polymerization with high spatiotemporal precision within cell-mimetic lipid vesicles known as giant unilamellar vesicles (GUVs). Within these active protocells, the reorganization of actin networks triggered outward membrane extensions as well as the unidirectional movement of GUVs at speeds of up to 0.43 µm/min, comparable to typical adherent mammalian cells. Notably, our findings reveal a synergistic interplay between branched and linear actin forms in promoting membrane protrusions, highlighting the cooperative nature of these cytoskeletal elements. This approach offers a powerful platform for unraveling the intricacies of cell migration, designing synthetic cells with active morphodynamics, and advancing bioengineering applications, such as self-propelled delivery systems and autonomous tissue-like materials.

Introduction

Motility is a fundamental property of cells across biological systems, from bacteria to large animals (*1*–*6*). By transcending the randomness and viscosity of the microscopic world, cells move toward their destination by extending membrane protrusions and by clutching onto the extracellular environment. These processes are universally galvanized by actin polymerization (*7*–*12*). While hundreds of biomolecules are identified to be required for cell motility (*4*, *6*, *13*), a minimal list of biomolecular components sufficient for cell motility remains elusive. This is primarily due to the self-evident challenge of eliminating all biomolecules but those minimal ones in the context of living cells.

Cell migration is driven by the coordination of forward movement, rear contraction, and adhesion/deadhesion of the cell edges (*4*, *6*, *14*–*16*). Among these processes, actin polymerization at the leading edge is a strong candidate for driving overall forward displacement. For instance, *Dictyostelium*, fish keratocyte, and human neutrophil retain their motility even after myosin contractility is compromised genetically (*17*, *18*) or pharmacologically (*19*, *20*). Cells also manage to migrate even without strong adhesions especially in confined conditions (*21*, *22*). Conversely, we and others have shown that synthetic activation of the Rho family GTPase Rac1, an upstream activator of the actin cytoskeleton, induces directional cell movements toward the site of stimulation (*23*, *24*). However, it is still unclear if Rac1-mediated actin polymerization alone is sufficient for cell motility in cellular settings, as Rac1 crosstalks to other Rho small GTPases such as RhoA and triggers other cytoskeletal activities including acto-myosin contraction (*25*).

In a different context, molecules necessary for force generation by actin polymerization have been identified based on the motility reconstitution assay (*26*–*35*). These reports demonstrated that a mixture of purified cytoskeletal proteins, such as actin, Arp2/3, profilin, cofilin, and capping protein, can reconstitute the motility of *Listeria monocytogenes* bacteria using microspheres coated with actin nucleation-promoting factors (NPFs). Furthermore, a number of studies were conducted to reconstitute actin (*36*, *37*) and other cytoskeletons (*38*–*40*) inside cell-sized membrane-bound liposomes. These studies demonstrated that the polymerization force of actin induces membrane deformations (*41*–*44*), reveals the roles of actin-binding proteins (*45*–*51*), and explores the regulation of internal reactions by light and external environmental factors (*51*–*54*). However, unidirectional motion by the cytoskeletal polymerization force has not been achieved. Moreover, non-invasive and non-constitutive—hence physiological—induction of actin polymerization has yet to be achieved, particularly within cell-sized compartments with proper membrane configuration. Collectively, we decided to develop a minimal membrane-bound system where actin molecules can be locally polymerized and to test if such an artificial cytoskeletal activity could induce cell-like motility.

Results

Reversible and asymmetric light control of protein localization inside GUVs

To achieve *in vitro* reconstitution of cell motility, we previously developed active protocells where chemically inducible dimerization (CID) tools were used to polymerize actin based on a bacterial NPF inside giant unilamellar vesicles (GUVs) (*55*). While the previous system efficiently produced actin polymerization, outward membrane extension necessary for driving movement was not observed. We reasoned that this was due to a lack of fast turnover of NPF recruitment to the membranes. To aim for a physiologically relevant generation of protrusive force exerted against membranes, we adopted a light-inducible protein dimerization tool for controlling the localization of proteins of interest. Among optogenetic dimerization tools (*56*–*58*), we chose iLID-SspB (*59*) due to its favorable characteristics, including molecular size, binding kinetics, and optical requirement, which are well-suited for experimental operations without compromising physiological relevance. More specifically, the second-timescale iLID photo-reaction is ideal for recapitulating the dynamic nature of migratory cells and their front-to-back polarization (Supplementary Text).

We first set out to test light-induced dimerization of purified iLID and SspB in GUVs. In our construct, iLID was membrane-tethered, and blue light exposure triggered the Jα helix to extend, revealing the binding site for SspB. In the dark, iLID returned to its closed state, releasing SspB (Fig. 1A). We monitored SspB localization changes and visualized the light response by fusing iLID with YFP and SspB with mCherry (Fig. S1A). To anchor iLID to the GUV membrane, we tested four different protein-lipid interaction strategies to mediate light-induced translocation, including coordination bonding, electrostatic, strong non-covalent, and covalent interactions (Fig. 1A) (*60*, *61*). These strategies were implemented using 6×His-tag/Ni-NTA-conjugated lipids, myristoylated alanine-rich C-kinase substrate-effector domain (MARCKS-ED)/phosphatidylserine (PS), 2×Strep-tag/StrepTactin/biotin-conjugated lipids, and SNAP-tag/benzylguanine (BG)-conjugated lipid, respectively (Fig. S2). While all four strategies successfully localized iLID-YFP to the membrane, MARCKS-ED/PS was less efficient in membrane-anchoring, and the His-tag/Ni-NTA and Strep-tag/StrepTactin/biotin systems showed some non-specific membrane binding of SspB before light illumination (Fig. S2). Thus, we primarily used SNAP/BG for most of the following experiments.

When GUVs were made with 2% BG-conjugated lipid in the inner leaflet, iLID localized on the membrane, while SspB remained in the lumen in the dark (Fig. 1B). Upon blue light illumination of the entire GUV, SspB translocated to the membrane within 4 seconds (Fig. 1B, C). After

112 switching back to the dark, SspB gradually dissociated from the membrane with a half-time of
113 61.2 ± 13.7 seconds. The time scale is consistent with AsLOV2 based-optogenetic tools
114 measured in cells (*57*). These data confirmed that iLID-SspB enables reversible control of
115 protein localization in GUVs.
116
117 Next, we tested the potential for spatially asymmetric control of iLID-SspB interactions. When
118 light was applied locally to one side of the GUV, SspB accumulated at the illuminated site (Fig.
119 1D, E). In the dark, dissociation proceeded with a half-time of 41.8 ± 7.1 seconds (Fig S3A).
120 Despite faster diffusion on artificial lipid membranes compared to cell membranes (*62–64*),
121 localized light stimulus created an asymmetric pattern of SspB in cell-sized vesicles (Fig. 1E, F,
122 see supplementary text). Furthermore, SspB precisely and repeatedly responded to the
123 directional change of blue light illumination (Figs. 1G, S3B, C, and Movie S1). Collectively, these
124 results demonstrated that the iLID-SspB system can direct polarized protein distribution at
125 regions of interest on the GUV membranes.
126
127 **Light-guided control of ActA**
128 Next, we sought to manipulate the actin cytoskeleton with the iLID-SspB system. Previous
129 studies have established that the rate of actin polymerization depends on the surface density of
130 NPFs (*26*, *30*, *35*) and that clustering of NPFs accelerates actin polymerization (*65*, *66*). We have
131 recently shown that chemically-induced membrane recruitment of ActA, an N-WASP homolog
132 NPF derived from *L. monocytogenes*, induces actin polymerization on the membrane of GUVs,
133 leading to symmetry breaking (*55*). Thus, we first tested ActA with the iLID-SspB system. By
134 testing two SspB variants with different affinities (SspB micro and SspB nano) and two fusion
135 orders (resulting in four ActA-SspB variants in total), we found that ActA-SspB$_{nano}$-mCherry
136 activates Arp2/3-dependent actin polymerization in bulk pyrene actin assays (Fig. S1, S4A, B)
137 and exhibits the best light-dependent membrane translocation without non-specific membrane
138 binding in the dark (Fig. S4C, D). When supplemented with actin and Arp2/3, light-induced
139 global membrane recruitment of ActA-SspB led to the emergence of actin patches on the
140 membrane, consistent with our previous findings with a chemical input (*55*) (Fig. S5). With local
141 light, ActA distribution became asymmetric, yet the directionality of actin polymerization could
142 not be maintained. In most cases, polymerized actin was randomly diffused out from the
143 illuminated region and the GUV lost actin directionality over time (Fig. S6 and Movie S2).
144
145 **Reversible control of pVCA and light-guided actin polymerization**
146 For robust maintenance of actin asymmetry, we set out to rapidly depolymerize actin filaments
147 in the non-illuminated area, providing precursor G-actin for new polymerization events. We
148 thus incorporated factors that facilitate the actin turnover process, namely profilin, cofilin, and
149 capping protein. Moreover, ActA could not induce membrane actin polymerization in GUVs in

the presence of cofilin and capping proteins (Fig. S7). We evaluated common NPFs to identify a more potent alternative to ActA. Among those tested, GST-tagged N-WASP pVCA (proline-rich region + VCA domain) showed the fastest actin polymerization in a bulk pyrene assay, which monitors actin polymerization through the florescence increase of pyrene-labeled actin. Notably, GST-pVCA maintained its activity when fused to SspB-mCherry fusion (Fig. 2A, S1, S8).

We then encapsulated this light-inducible pVCA-SspB-mCherry with actin (10% Alexa-647 labeled), Arp2/3, profilin, cofilin, and capping protein in GUVs (Fig. 2B). Upon illumination, pVCA-SspB-mCherry rapidly translocated to the membrane, followed by the increase of membrane actin signal, suggesting light-induced actin polymerization (Fig. 2C–E, Movie S3). In contrast, in the absence of either pVCA or light stimuli, no significant change in membrane actin intensity was observed (Fig. 2D, E, Fig. S9). When Arp2/3 was omitted, the membrane actin signal showed a slight increase over time. This suggested that the G-actin binding property of pVCA (*67*, *68*) increased local concentration of the G-actin at the periphery of membrane and facilitated spontaneous polymerization, which was not as intense as Arp2/3-dependent actin polymerization (Fig. 2D, E, Fig. S9). Taken together, these data suggested that light-dependent membrane accumulation of pVCA induces Arp2/3-dependent actin polymerization on the GUV membrane.

Next, we tested the reversibility of the actin polymerization. As shown in Fig. 2F and G, both pVCA-SspB-mCherry and actin reversibly and repetitively changed their intensity on the membrane depending on blue light switching (Movie S4). Notably, once switched to the dark, pVCA-SspB-mCherry quickly dissociated from the membrane, whereas actin decreased its membrane intensity at a relatively slower rate (Fig. S10). This delay in actin response suggested that actin was not simply sequestered by pVCA dissociation, but was rather gradually depolymerizing. Furthermore, when the system responded to the next round of blue light illumination, actin signal increased slightly slower than pVCA-SspB, supporting that a substantial fraction of actin filaments disassembled in the dark and re-polymerized upon new stimulus (Fig. S10). Together, these results suggested that the polymerization state is reversible in our system and that the balance between polymerization and depolymerization can be controlled by light.

Asymmetric and spatially controlled actin polymerization

The polarity of NPFs and actin polymerization are fundamental features of directed cell migration (*9*, *69*, *70*). Thus, we next tested whether locally targeted pVCA could establish asymmetric actin polymerization (Fig. 3A). As shown in Fig. 3B, C, and Fig. S11A, pVCA showed asymmetric patterning toward the localized light stimulus (Movie S5). About 5 minutes after pVCA translocation, the actin signal also increased from the illuminated region and created an asymmetric pattern. Furthermore, with continuously applied local light, both pVCA and actin

maintained their polarity for more than 100 minutes (Fig. 3B, C, S11A, Movie S5). We note that the actin signal appeared as two lines in the latter time points in the kymograph. This is possibly because actin filaments are less diffusive on the membrane, and so Alexa-647 labeled on actin molecules was gradually photo-bleached by blue light excitation. Next, we tested if the system reversibly changed the direction of actin polymerization. After establishing an asymmetric actin pattern with a local light on the right side of the vesicle, we reversed it back to the dark mode and subsequently shed new light on the left. pVCA and actin responded accordingly to re-polarize toward the new signal site (Fig. 3D, E, and Movie S6). These data demonstrated that the light-inducible pVCA system can establish polarized actin patterns in a reversible manner.

Importantly, when locally illuminated, the front membrane of some GUVs moved toward the light direction (Fig. S11B), albeit occasionally (2 out of 7 instances). We speculate that characteristics inherent to the GUV system such as surface-to-volume ratio of individual GUVs, surface density of pVCA, and the ratio between Arp2/3 and capping protein (*33*, *71*), as well as any combination of these factors might be critical in determining a functional output.

mDia1-driven actin polymerization drives efficient membrane protrusions in cells

To enhance forward membrane protrusion, we next sought to reinforce actin polymerization. At the leading edge of migrating cells, two major actin nucleators, namely Arp2/3 and formin, coordinate the forward extension of the plasma membrane (*72*–*74*). While Arp2/3 stays at the branch points of the actin filaments and does not engage in the incorporation of monomeric actin into the growing ends, formin continuously binds to the growing ends and actively recruits profilin-actin complexes to the elongating tips. Consequently, one subtype of formin, mDia1, accelerates actin polymerization 4–5 times faster (*75*, *76*) and drives motility 6–23 times faster than Arp2/3 in *in vitro* motility assays using functionalized beads (*30*, *28*, *31*). Furthermore, a theoretical study suggests that actin polymerization perpendicular to the membrane, characteristic of formin-driven filopodia formation, more efficiently transduces the polymerization force to advance the membrane (*77*). Therefore, we reasoned that the integration of mDia1 could enhance protrusive activity.

In line with our previous actin-actuation tool development (*78*), first, we used living cells to test if membrane recruitment of mDia1 could induce actin polymerization and membrane protrusions in a three-dimensional lipid bounded context (Fig. S12A) (*79*–*81*). More specifically, we took FH1-FH2-DAD domains from mDia1 as a constitutively active form (*82*) and recruited it to the plasma membrane by the CID system. As shown in Fig. S12B–H, rapamycin-dependent plasma membrane translocation of YF-mDia1 induced filopodia-like protrusions (Fig. S12B–H). These protrusions were positive for Lifeact signal and showed coiling motions with their

elongating tips labeled with YF-mDia1 (Fig. S12D), replicating the previously reported phenotypes of formin-dependent filopodia elongation (*83–86*). These data supported that membrane translocation of mDia1 generates an actin-dependent protrusive force on the membrane.

mDia1-driven actin polymerization drives forward movement of GUVs

We then constructed the light-inducible version of mDia1 (mCherry-SspB-mDia1) (Fig. S1, S8) and encapsulated it with iLID-YFP-SNAP, actin (10% Alexa-647 labeled), profilin, and cofilin in GUVs. Upon local recruitment of mDia1, some vesicles showed gradual drift toward the stimulated direction, suggesting that mDia1 exerted protrusive forces also in the reconstituted lipid vesicles (Fig. S13A, B). However, the response was minimal and difficult to detect. Therefore, aiming to better mimic the actin network of migrating cells, we added pVCA-SspB, Arp2/3, and capping protein (Fig. 4A). Remarkably, this full component system (pVCA + mDia1) showed robust movements toward light stimulation, as observed in 18 out of 22 GUVs (Fig. 4B–D, Fig. S13C–E, Movie S7, S9, S10). Polarized actin signal toward the illuminated direction suggested that actin polymerization provided the force to push the membrane forward (Fig. 4B, Movie S7). The vesicle continued to move steadily for an hour until the light was turned off (Fig. 4B, D, Movie S7). Furthermore, when we shifted the position of the blue light, the signals for mDia1, pVCA, and actin reoriented, causing the vesicle to move in the new direction, akin to how a migrating neutrophil responds to a new chemoattractant (Fig. 4B, D, Movie S7). The speed of pVCA/mDia1 dual system was roughly 3 times larger than that of mDia1 GUVs (Fig. 4F, S13B–D). The distance the front side membrane moved in 30 minutes was also significantly longer in pVCA + mDia1 GUVs (Fig. S13E). Furthermore, membrane recruitment of mDia1 and pVCA occasionally showed local protrusions, suggesting the generation of protrusive force (Fig. S14, Movie S8). Together, the data indicated that mDia1-driven actin polymerization exhibits a protrusive force that is substantially enhanced by pVCA and Arp2/3.

When mDia1 and pVCA were replaced with the same amount of mCherry-SspB, vesicles did not move even with the local blue light illumination (Fig. S15). In addition, the kymographs of the protrusions of the vesicle perimeter and the membrane actin intensity indicated the timing and direction of membrane protrusions correlate to the actin intensity and its polarity, supporting that membrane protrusion is driven by actin cytoskeleton (Fig. 4D, E). Corroborating this, the actin sequestering compound Latrunculin A and the formin inhibitor SMIFH2 substantially compromised motility (Fig. 4H). Furthermore, deletion of the DAD domain from mDia1, which is responsible for efficient actin nucleation by mDia1 (*87*), abolished the motility (Fig. 4H). These results indicate that membrane protrusion and motion of the vesicles are driven by actin polymerization.

Deformation and adhesion of GUVs

Although the vesicles initially moved at an average velocity of 0.43 µm/min, their speed gradually decreased over time (Fig. 4F, G, Fig. S13C, D). Concomitant with this deceleration, the contact area of the bottom side of the vesicles constantly increased during the movement, stabilizing the vesicles in a dome-like shape (Fig. 4C, I). This increase in the contact area was not seen in the GUVs when pVCA and mDia1 were replaced with mCherry-SspB (Fig. S15). Thus, we speculate that the contact to the bottom substrate was induced by the protrusive reaction and that the adhesion and the concomitant deformation led to cumulative tension increase (*88*) which in turn counteracted the protrusive force. The force exerted by actin polymerization may not be enough to detach the GUV from the BSA-coated glass substrate. This is consistent with the observation where an initial contact site remained adherent even in a GUV that traveled farthest (Fig. 4I, Fig. S16A, B, Movie S9, S10). Additionally, actin recycling in the system may be insufficient and force gradually diminishes over time (*89*). Despite these potential resisting factors, the combination of mDia1 and pVCA induced movement consistently (Fig. 4, Fig. S13C, S16). Thus, we concluded that the asymmetric actin polymerization mediated by pVCA-mDia1 is sufficient to propel the vesicles forward from within.

Discussion

In the present study, we developed a fully reconstituted protocellular system to achieve light-directed motility in a protocell. We leveraged mDia1-mediated actin polymerization to establish the forces that drive movement. Our findings not only corroborate recent cell biological findings on formin's significant roles in cell migration (*83*, *90–95*) but also uniquely demonstrate that the mDia1-mediated actin polymerization system is sufficient to propel lipid vesicles, overcoming challenges thus far posed by genetic redundancy and cellular complexity. Formin-mediated actin polymerization exhibits several unique features compared to free barbed end elongation in Arp2/3-dependent polymerization, including processive elongation (*31*, *75*), accelerated polymerization rate (*75*, *76*), rotation, and coiling motion (*85*, *86*, *96*). These characteristics could contribute to the effective propulsion of the vesicle. Remarkably, our minimal system further revealed a significant synergy between pVCA and mDia1. Although further investigation is required, this synergistic effect may be explained by a positive feedback loop: mDia1 functions both as an actin elongator and a supplier of mother filaments for Arp2/3-mediated actin polymerization (*91*, *93*). In return, branch formation by the Arp2/3 complex likely generates more growing filaments for mDia1 to bind and elongate. To further elucidate the mechanisms of force generation and membrane protrusion, unveiling the nanoscopic architecture of the actin network in the migrating protocell will be crucial. Our protocell approach, which bridges the gap between cellular and biochemical domains, opens new avenues for comprehensively interrogating modules of cellular motility.

We achieved a GUV displacement speed in the range of 0.1–1.0 µm/min, which is comparable to the migration rates of typical fibroblasts (*97*) and other adherent cells including those that competed in the World Cell Race (*98*). How could we make the movement even faster? *L. monogytogenes* and NPF-coated beads in purified cytoskeletal protein solution typically move in the range of 1–15 µm/min (*27*, *28*, *30*–*33*). Some adherent cells can migrate at 5 µm/min even when actomyosin contractility is inhibited (*19*). We propose three possible ways to make artificial cell migration faster. First, increasing actin concentration (*76*, *99*) and integrating additional factors, such as VASP (*100*), Fascin (*101*), and NPFs (*66*, *102*), could accelerate the rate of actin polymerization. Secondly, optimizing membrane tension could enhance the deformability of the lipid membrane, akin to the malleable structures observed in motile cells, thereby potentially promoting more efficient protrusion and motility (*49*, *103*). Finally, fine-tuning adhesion could enhance migration efficiency as many cells exhibit a preference for an optimal adhesion range, where both insufficient and excessive adhesion can hinder motility (*104*, *105*).

Interestingly, the phenotypes of mDia1 membrane recruitment differed between cells and GUVs. In cells, mDia1 produced filopodia-like thin protrusions (Fig. S12), whereas in GUVs, it pushed the lipid membrane as a continuous plane at a much broader scale than filopodia (Fig. 4, S13–16). Since living cells tend to have higher membrane tension than liposomes (*106*), it may appear counterintuitive that the cell membrane was more susceptible to mDia1-induced local deformation. One possible explanation is that, in cells, endogenous proteins might work in concert with mDia1 to amplify local membrane deformation and form long filopodia-like protrusion. For Instance, SH3-containing proteins including IRSp53 (*107*) and Abi1 (*91*) could interact with the proline-rich FH1 domain of mDia1. Alternatively, localized defects in membrane tension could predispose certain areas to form thin protrusions (*108*). Additionally, cytoskeleton-bound transmembrane proteins impede tension propagation in cells (*109*). Furthermore, the nuclear accumulation of mDia1 in cells (Fig. S12) could reduce its effective concentration and cause a heterogeneous distribution on the cell membrane, resulting in focused protrusive force in regions with high mDia1 concentration, similar to how pVCA-driven finger-like protrusions are formed in liposomes, as demonstrated by Gat *et al.* (*110*). Seamlessly bridging native and artificial cells would be critical for a comprehensive understanding of the regulatory mechanism of cellular morphodynamics.

We have recently shown that chemically-induced membrane recruitment of ActA, an NPF derived from *L. monocytogenes*, and subsequent global actin polymerization lead to eccentricity in the shape of GUVs (*55*). We noted a difference in membrane deformation between the CID and LID systems, as the CID too could induce a clear membrane deformation

given a global, non-directional input. This difference could be attributed to the variations in cytoskeletal proteins and input signals between the two systems. In the present study, we have incorporated cofilin and capping proteins. Since cofilin and capping protein accelerate actin depolymerization, these factors may make the actin network more plastic rather than exert force to deform the membrane. Moreover, the binding kinetics of iLID-SspB (k_{on} =1.2 × 10^3 $M^{-1}s^{-1}$, k_{off} =1.1 × 10^{-3} s^{-1}, K_d = 0.8 μM) substantially differs from that of FKBP-FRB (k_{on} =1.9 × 10^6 $M^{-1}s^{-1}$, k_{off} =2.2 × 10^{-2} s^{-1}, K_d = 12 nM) (*59*, *111*, *112*). This may result in different reaction dynamics between actin cytoskeleton and the lipid membrane.

Our finding that internal cytoskeletal force can drive the unidirectional motion of lipid vesicles would offer avenues to reverse-engineer cell motility. Although we used light as an input, asymmetric actin polymerization may be achievable with chemical inputs with consideration of binding affinity (*79*, *113*), transmembrane signal transduction mechanisms (*114*), and self-organized pattern formation (*115*–*119*). Furthermore, combining this approach with other migratory forces (*111*, *120*, *121*) and applying synthetically engineered cytoskeletal molecules (*76*, *122*) could enhance the motility even beyond the limit of natural systems. Achieving synthetic motility in GUVs could be a step toward future developments in active therapeutic agents, self-organizing artificial tissues, and synthetic neural circuits.

Materials and Methods

Reagents

ATP was purchased from Gold Biology (A-081) or Nacalai Tesque (01072-82), prepared as 100 mM solution in 100 mM Tris-HCl (pH 7.4 at RT), and stored at -20°C. Creatin phosphate was purchased from Gold Biotechnology (C-323-5) or Oriental Yeast (45180000), prepared as 1 M solution in PBS (Gibco 10010-023), stored at -20°C. Creatin kinase was purchased from Sigma-Aldrich (10127566001) or Oriental Yeast (46430003), prepared as 40 µM solution in buffer V (50 mM HEPES-NaOH (pH 7.5), 150 mM NaCl, 7 mM β-mercaptoethanol, 10% glycerol), snap frozen, and stored at -20°C. Flavin mononucleotide (FMN) was purchased from TCI (R0023) and Wako (06500171), freshly prepared as 600 µM solution in MilliQ water before iLID expression. Alexa Fluor 647 C2 Maleimide (A20347) and Pierce™ Glutathione Agarose (16100) were purchased from Thermo Fisher Scientific. Hexadecane (H6703), Silicone oil (378348), and SMIFH2 (S4826) were purchased from Sigma-Aldrich. Latrunculin A was purchased form Wako (125-04363). Benzylguanine-PEG2000-DSPE was prepared and purified as previously described (*60*). POPC (1-palmitoyl-2-oleoyl-glycero-3-phosphocholine, 850457), POPS (1-palmitoyl-2-oleoyl-sn-glycero-3-phospho-L-serine, 840034), 18:1 DGS-NTA-Ni (1,2-dioleoyl-sn-glycero-3-[(N-(5-amino-1-carboxypentyl)iminodiacetic acid)succinyl] (nickel salt), 790404), 18:1 PE-PEG2000-benzylguanine (1,2-dioleoyl-sn-glycero-3-phosphoethanolamine-N-[benzylguanine(polyethylene glycol)-2000], 880137), and 18:1 Biotinyl Cap PE (1,2-dioleoyl-sn-glycero-3-phosphoethanolamine-N-(cap biotinyl) (sodium salt), 870273C) were purchased from Avanti Polar Lipids as chloroform solution. Actin (AKL99), pyrene labeled actin (AP05), Arp2/3 (RP01P), Profilin (PR02), Cofilin (CF01), were purchased from Cytoskeleton. Strep-Tactin XT (2-4010-010, discontinued) resin, Strep-Tactin XT 4Flow (2-5010-010) resin, and purified Strep-Tactin protein were purchased from IBA. Ni-NTA agarose (30210) was purchased from Qiagen. Amylose resin (E8021S) was purchased from New England BioLabs.

Plasmid construction

pQE80L-6×His-MBP-TEVprorease(S219V)

Ser219Val mutation (*123*) was introduced by PCR with the template plasmid gifted from Dr. Yubin Zhou and the primer set of fwd: 5’-TGGTGAAACCTGAAGAACCTTTT-3’ and rev: 5’-TTCACCATGAAAACTTTATGGCC-3’. TEV prorease (S219V) was then PCR amplified with the primer set of fwd: 5’-AATTGAGCTCGATGAGCGGCCTGGTGC-3’ and rev: 5’-AATTGGATCCTTATTGCGAGTACACCAATTCATTCATG-3’ and inserted between SalI and BamHI sites of pQE-80L MBP-SspB Nano plasmid (Addgene #60409) by using restriction digestion and T4 ligase ligation process.

pQE80L-6×His-MBP-TEVsite-mCherry-SspB(micro)

EYFP-2×SAGG linker was PCR amplified from the template plasmid YFP-FKBP (*124*)with the primer set fwd: 5’- GTATTTTCAGGGATCGCCGCTAGCGCTACCGG-3’ and rev: 5’- TCGGGGAGCTGGATCCTCCGCCAGCGCTGC-3’ and inserted into BamHI site of pQE-80L MBP-SspB Nano plasmid (Addgene #60409) by using Gibson assembly. EYFP part was then replaced with mCherry from pmCherry-C1 (Clontech) by restriction digestion and T4 ligase ligation process with AgeI and BsrGI. Arg73 of SspB was mutated to Gln by PCR with the primer set fwd: 5’- AACGCCCagTTTAAGGGCGTGTCTCGT-3’ and rev: 5’- CTTAAActGGGCGTTGAACTGGATAA-3’.

pGEX-2T-GST-3Csite-TEVsite-6×His

Two sets of oligo DNA pairs were designed to introduce 3C protease cleavage site, TEV protease cleavage site, and 6×His tag (1st set, fwd: 5’- GGTTCCGCGTGGATCTGGTCTTGAGGTGCTCTTTCAGGGACCCGGCAGTCTCGAGGGTCTGTACAAGCG AATTCAG-3’, rev: 5’- CTGAATTCGCTTGTACAGACCCTCGAGACTGCCGGGTCCCTGAAAGAGCACCTCAAGACCAGATCCACG CGGAACC-3’. 2nd set, fwd: 5’- TACAAGCGAATTCAGGAGAACCTCTACTTTCAAAGCGATCATCATCATCATCATCACTAAAAATTCATCGT GACTG-3’ and rev: 5’- CAGTCACGATGAATTTTTAGTGATGATGATGATGATGATCGCTTTGAAAGTAGAGGTTCTCCTGAATTCG CTTGTA-3’ (underlines indicate overhang sequences)). To anneal oligo DNAs individually, 0.5 µM each DNAs were mixed in 1× T4 Ligase buffer (NEB, B0202S) and heated at 85°C for 10 min and cooled 5°C per 2 min down to 40°C. pGEX-2T, which was kindly gifted from Dr. Miho Iijima, was digested by BamHI and EcoRI and assembled with the two annealed DNA fragments by Gibson assembly.

pGEX2T-GST-pVCA-3Csite-SspB(micro)-mCherry-TEVsite-6×His

To first construct pGEX2T-GST-pVCA-3Csite-TEVsite-6×His, pVCA (proline rich region and VCA domain) of human N-WASP was PCR amplified with the primer set fwd: 5’- CAGTCTCGAGGGAGGTGTTGAAGCTGTTAAAAATGA-3’ and rev: 5’- TCCTGAATTCCGTCTTCCCACTCATCATCATCCTC-3’ and inserted between XhoI and EcoRI site of pGEX-2T-GST-3Csite-TEVsite-6×His by using restriction digestion and T4 ligase ligation. Then, SspB(micro)-mCherry was PCR amplified with the primer set fwd: 5’- TGAGTGGGAAGACGGAATTGGGCAGTCGACGGTACCGCG-3’ and rev: 5’- GTAGAGGTTCTCCTGAATTCCCTTGTACAGCTCGTCCATGCC-3’ and inserted in the EcoRI site of pGEX2T-GST-pVCA-3Csite-TEVsite-6×His by Gibson assembly.

pET28-2×Strep-iLID-EYFP-MARCKS

First, pET28-2×Strep-iLID-6×His was constructed as follows. iLID sequence was cut out from the pLL7.0: Venus-iLID-Mito (Addgene #60413) by NheI and EcoRI and inserted between NheI and EcoRI sites of pET28-2×Strep-tag gifted from Dr. Kanemaki by using restriction digestion and T4 ligase ligation. Then, to construct pET28-2×Strep-iLID-EYFP-6×His, EYFP was PCR amplified from pEYFP-C1 (Clontech) with the primer set fwd: 5'-AATTGTCGACATGGTGAGCAAGGGCGAG-3' and rev: 5'-AATTGCGGCCGCCTTGTACAGCTCGTCCATGC-3' and inserted between SalI and NotI sites of pET28-2×Strep-iLID-6×His by restriction digestion and T4 ligation. MARCKS-ED fragment was constructed by oligo annealing (1st set fwd: 5'-GTACAAGGGAAGTGCTGGTGGTAAAAAGAAAAAGAAGCGCTTTTCCTTC-3' and rev: 5'-TTCTTGAAGGAAAAGCGCTTCTTTTTCTTTTTACCACCAGCACTTCCCTT-3', 2nd set fwd: 5'-AAGAAGTCTTTCAAGCTGAGCGGCTTCTCCTTCAAGAAGAACAAGAAGTA-3' and rev: 5'-GTACTACTTCTTGTTCTTCTTGAAGGAGAAGCCGCTCAGCTTGAAAGAC-3') and inserted into BsrG1 site of pET28-2×Strep-iLID-EYFP-6×His.

pET28-2×Strep-iLID-EYFP-SNAP

SNAP tag sequence was PCR amplified from the template Phage-ubc-nls-ha-tdMCP-SNAP, a kind gift from Dr. Bin Wu, with the primer set fwd: 5'-AATTTGTACAAGTCTGCTGGCGGAAGCGCTGGAGGCAGCATGGACAAAGACTGCGAAATGAAGC-3' and rev: 5'-AATTGCGGCCGCTTAACCCAGCCCAGGCTTG-3' and inserted between BsrGI and NotI of pET28-2×Strep-iLID-EYFP-MARCKS by restriction digestion and T4 ligation.

iLID-EYFP-CAAX (Clontech C1) and iLID mutants

iLID-EYFP sequence was cut out from pET28-2×Strep-iLID-EYFP-6×His by NheI and BsrGI and inserted between NheI and BsrGI sites of FRB-ECFP-CAAX (*125*) by using restriction digestion and T4 ligation.

mCherry-SspB(micro) (Clontech C1)

SspB(micro) sequence was PCR amplified from pQE80L-6×His-MBP-TEVsite-mCherry-SspB(micro)
with the primer set fwd: 5'-GAACAGTACGAACGCGCC-3' and rev: 5'-AATTCTCGAGGACCACCAGCACTACCACCAGCACTACCACCAGCACTACCACCAGCACTACCACCAGCAC
TACCAATATTCAGCTCGTCATAGATT-3' and inserted between BsrGI and XhoI sites by restriction digestion and T4 ligation. A silent mutation was introduced to BamHI site upstream of SspB by inverse PCR with the primer set fwd: 5'-GAGGATCtAGCTCCCCGAAACGCCCT-3' and rev: 5'-GGGAGCTaGATCCTCCGCCAGCGCTG-3'

pQE80L-MBP-TEVsite-mCherry-MCS

mCherry sequence was PCR amplified from pmCherry-C1 (clontech) with the primer set fwd: 5'-GTATTTTCAGGGATCGCTAGCGCTACCGGTC-3' and rev: 5'-TCAGCTAATTAAGCTATCAGTTATCTAGATCCGGTGGATC-3' and inserted between BamHI and HindIII sites of pQE-80L MBP-SspB Nano by Gibson assembly.

2×Strep-mCherry-MCS

mCherry sequence was PCR amplified from pmCherry-C1 (clontech) by the primer set fwd: 5'-AGCGGGTGCCGCTAGTCATATGGGTACGCTAGCGCTACCGGTCG-3' and rev: 5'-GGTGGTGGTGCTCGATCAGTTATCTAGATCCGGTGGATCC-3' and inserted between NheI and XhoI sites of pET28-2×Strep-tag by Gibson assembly.

2×Strep-MBP-TEVsite-mCherry-MCS

MBP-TEVsite-mCherry-MCS was PCR amplified from the template pQE80L-MBP-TEVsite-mCherry-MCS with the primer set fwd 5'-CAAATGGGTCGGATCGACGGATCTAAAATCGAAGAAGG-3' and rev: 5'-GGTGGTGGTGCTCGATCAGTTATCTAGATCCGGTGGA-3' and inserted between BamHI and XhoI sites of pET28-2×Strep-tag by Gibson assembly.

pCold-6×His-2×Strep-MBP-TEVsite-mCherry-SspB(micro)-mDia1(FH1-FH2-DAD)

A DNA fragment 2×Strep-MBP-TEVsite-mCherry was PCR amplified from 2xStrep-MBP-mCherry-MCS with the primer set fwd: 5'-TCGAAGGTAGGCATATGGGCTGGTCTCACCC-3' and rev: 5'-ACAGCTCGTCCATGCCG-3'. The other DNA fragment SspB(micro) was PCR amplified from mCherry-SspB(micro) (Clontech C1) with the primer sets fwd: 5'-GCATGGACGAGCTGTACAAG-3' and rev: 5'-TCATTCTTGGCCATAGCTTGAGCTCGAGGACC-3'. pCold-mDia1, which was a kind gift from Dr. Roberto Dominguez, was digested by NdeI and assembled with the two DNA fragments by Gibson assembly.

pET28-2×Strep-mCherry-SspB(micro)-mDia1(FH1-FH2-DAD)

mCherry-SspB(micro)-mDia1(FH1-FH2-DAD) was cut out from pCold-6×His-2×Strep-MBP-TEVsite-mCherry-SspB(micro)-mDia1(FH1-FH2-DAD) by AgeI and BamHI and inserted between AgeI and BamHI sites of 2×Strep-mCherry-MCS by restriction digestion and T4 ligation.

EYFP-FKBP-mDia1(FH1-FH2-DAD)

mDia1(FH1-FH2-DAD) was cut out from pCold-6×His-2×Strep-MBP-TEVsite-mCherry-SspB(micro)-mDia1(FH1-FH2-DAD) by XhoI and BamHI and inserted between XhoI and BamHI of EYFP-FKBP by restriction digestion and T4 ligation.

pET28-6×His-2×Strep-TEVsite-Capβ2(mouse)-Capα1(mouse)

First, pET28-6×His-2×Strep was constructed as follows. 6×His sequence was synthesized by oligo annealing of fwd: 5'-AGGAGATATACCATGGGCCATCACCATCACCATCACATGGGCTGGTCTCA-3' and rev: 5'- TGAGACCAGCCCATGTGATGGTGATGGTGATGGCCCATGGTATATCTCCT-3' and inserted into NcoI site of pET28-2×Strep-tag. Capβ2(mouse)-Capα1(mouse) was PCR amplified from the template of pET3d-Capβ2(mouse)-Capα1(mouse), gifted from Dr. Julie Plastino and Dr. Cecile Sykes, with the primer set fwd: 5'-CTGGAGCGGGTGCCGCTAGCGAGAACCTCTACTTTCAAAGCGATATGAGCGATCAGCAGCTGG-3' and rev: 5'- TGTCGACGGAGCTCGAATTCTTAAGCATTCTGCATTTCTTTGCCAATC-3' and inserted between NheI and EcoRI of pET28-6×His-2×Strep by Gibson assembly. TEV cleavage site was designed in the forward primer and introduced between 2×Strep tag and Capβ2 ORF.

Actin preparation

Actin for GUV experiments was reconstituted from lyophilized powder as described in manufacturer's instructions, aliquoted, snap-frozen in liquid nitrogen, and stored at -80°C.

For actin polymerization assays, actin was dissolved in G-buffer [2 mM Tris-HCl (pH 7.5 at RT), 0.1 mM $CaCl_2$, 0.2 mM ATP, 0.5 mM DTT, 1 mM NaN_3] at concentration less than 65 µM and dialyzed against G-buffer for 3 days with daily buffer exchange. Dialyzed actin was then purified by a Superdex 200 increase 10/300 GL column (Cytiva) to separate monomer fraction from occasional larger molecular size (smaller elution volume) fraction. The purified actin was stored at 4°C with dialysis against G-buffer. The dialysis buffer for actin storage was exchanged twice a week**.**

Alexa 647 labeling of actin was performed following the previously reported method (*126*). First, rabbit skeletal muscle actin (Cytoskeleton Inc., #AKL99) was dissolved in G*-buffer [2 mM Tris-HCl (pH 7.5 at RT), 0.1 mM $CaCl_2$, 0.2 mM ATP] at concentration less than 65 µM and dialyzed against G*-buffer overnight and 3 hours. Dialyzed actin was collected and mixed with 4 molar excess Alexa Fluor 647 C2 maleimide (ThermoFisher, A20347, solubilized to 10 mM in DMSO) and incubated at 4°C overnight with rotation (10 min labeling as in the original protocol did not yield efficient labeling in the case of Alexa Fluor 647). The reaction was quenched by adding DTT to 10 mM. aggregated proteins and insoluble dyes were removed by ultracentrifugation at 350,000×g (90,000 rpm, TLA-100.1 rotor) for 12 min. The supernatant was collected and mixed 1/10 volume of 10×KMEI buffer (500 mM KCl, 10 mM $MgCl_2$, 10 mM EGTA, 100 mM Imidazole, pH 7.0) and final 1 mM ATP to polymerize actin at RT for 2–3 hours. Labeled filamentous actin was collected by ultracentrifugation at 195,000×g (67,000 rpm, TLA-100.1 rotor) for 30 min and resuspended with G-buffer. The labeled actin was dialyzed against G-buffer for 3 days with daily buffer exchange and purified through size exclusion chromatography with a Superdex 200 increase 10/300. The protein was snap-frozen in liquid nitrogen and stored at -80°C.

Protein purification

All protein expressions were carried out in BL21-CodonPlus (DE3)-RIL (Agilent Technologies). Cell lysis was performed by microfluidizer (Microfluidics, Model M-110Y).

6×His-MBP-TEV protease (S219V)

The bacteria transformed with pQE80L-6×His-MBP-TEVprotease (S219V) were cultured overnight in LB broth supplemented with 100 µg/mL Ampicillin and 25 µg/mL Chloramphenicol (LB/Amp/Cam). Pre-culture was inoculated to LB/Amp/Cam and cultured at 37°C until OD_{600} reached around 0.4. Protein expression was induced by adding 300 µM IPTG and allowed to proceed for 17 hours at 18°C. The cells were re-suspended with 50 mM Tris-HCl (pH 7.5 at RT), 250 mM NaCl, 5 mM $MgCl_2$, 7 mM β-mercaptoethanol and lysed by microfluidizer. The lysate was centrifuged at 20,000×g at 4°C for 30 min to remove cell debris. The protein was purified by Ni-NTA, eluted around 60–100 mM imidazole, and then dialyzed against 25 mM Tris-HCl (pH 7.5 at RT), 200 mM NaCl, 7 mM β-mercaptoethanol. The elution was concentrated by Amicon Ultra (10 kDa cutoff) and further dialyzed against 25 mM Tris-HCl (pH 7.5 at RT), 200 mM NaCl, 7 mM β-mercaptoethanol, 50% glycerol. The protein was stored at -20 °C.

mCherry-SspB

The bacteria transformed with pQE80L-6×His-MBP-TEVsite-mCherry-SspB were cultured overnight in LB broth supplemented with 100 µg/mL Ampicillin and 25 µg/mL Chloramphenicol (LB/Amp/Cam). Pre-culture was inoculated to LB/Amp/Cam and cultured at 37°C until OD_{600} reached 0.4–0.6. Protein expression was induced by adding 300 µM IPTG and allowed to proceed for 18 hours at 22°C. The cells were re-suspended with 50 mM Tris-HCl (pH 7.5 at RT), 250 mM NaCl, 7 mM β-mercaptoethanol, 20 mM Imidazole supplemented with cOmplete EDTA-free protease Inhibitor Cocktail (MilliporeSigma) and lysed by microfluidizer. The lysate was centrifuged at 20,000×g at 4°C for 30 min to remove cell debris. The protein was first purified by Ni-NTA, eluted around 50 mM imidazole, and then dialyzed against 25 mM Tris-HCl (pH 7.5 at RT), 250 mM NaCl, 7 mM β-mercaptoethanol. 6×His-MBP tag was cleaved by 6×His-MBP-TEV protease (S219V) (purified in house) during the dialysis. The cleaved 6×His-MBP tag and TEV protease were removed through the second round of Ni-NTA column. Flow through and wash fractions were dialyzed against buffer S [25 mM Tris-HCl (pH 7.5 at RT), 250 mM NaCl, 7 mM β-mercaptoethanol] and concentrated by Amicon Ultra (10 kDa cutoff). The protein was snap-frozen in liquid nitrogen in storage buffer [25 mM Tris-HCl (pH 7.5 at RT), 250 mM NaCl, 7 mM β-mercaptoethanol, 20% glycerol] and stored at -80 °C.

iLID-YFP-MARCKS

The bacteria transformed with pET28-2×Strep-iLID-EYFP-MARCKS were cultured overnight in LB broth supplemented with 50 µg/mL Kanamycin and 25 µg/mL Chloramphenicol (LB/Kan/Cam). Pre-culture was inoculated to LB/Kan/Cam and cultured at 37°C until OD600 reached around

0.6. Protein expression was induced by adding 300 µM IPTG and allowed to proceed for 17 hours at 23°C in the presence of 6 µM FMN. The cells were resuspended with buffer L1 [50 mM Tris-HCl (pH 7.5 at RT), 200 mM NaCl, 1 mM EDTA, 7 mM β-mercaptoethanol] and lysed by microfluidizer. The lysate was centrifuged at 20,000×g at 4°C for 30 min to remove cell debris. The supernatant was applied to Strep-Tactin XT (IBA Lifesciences) equilibrated with buffer L1 and the protein was eluted with 50 mM biotin in buffer L1. The elution was dialyzed against buffer L2 [25 mM Tris-HCl (pH 7.5 at RT), 200 mM NaCl, 7 mM β-mercaptoethanol] and concentrated by Amicon Ultra (10 kDa cutoff). The protein was snap-frozen in liquid nitrogen in storage buffer [25 mM Tris-HCl (pH 7.5 at RT), 200 mM NaCl, 7 mM β-mercaptoethanol, 30% glycerol] and stored at -80 °C.

iLID-YFP-SNAP

The bacteria transformed with pET28-2×Strep-iLID-EYFP-SNAP were cultured overnight in LB broth supplemented with 50 µg/mL Kanamycin and 25 µg/mL Chloramphenicol (LB/Kan/Cam). Pre-culture was inoculated to LB/Kan/Cam and cultured at 37°C until OD_{600} reached around 0.5. Protein expression was induced by adding 300 µM IPTG and allowed to proceed for 20 hours at 23°C in the presence of 6 µM FMN. The cells were resuspended with buffer L1 (50 mM Tris-HCl (pH 7.5 at RT), 200 mM NaCl, 1 mM EDTA, 7 mM β-mercaptoethanol) and lysed by microfluidizer. The lysate was centrifuged at 20,000×g at 4°C for 30 min to remove cell debris. The supernatant was applied to Strep-Tactin XT (IBA Lifesciences) equilibrated with buffer L and the protein was eluted with 50 mM biotin in buffer L1. The elution was further purified by Superdex 200 increase 10/300 GL column in the buffer L2 [25 mM Tris-HCl (pH 7.5 at RT), 200 mM NaCl, 7 mM β-mercaptoethanol] and concentrated by Amicon Ultra (10 kDa cutoff). The protein was snap-frozen in liquid nitrogen in storage buffer [25 mM Tris-HCl (pH 7.5 at RT), 200 mM NaCl, 7 mM β-mercaptoethanol, 30% glycerol] and stored at -80 °C.

GST-pVCA-SspB-mCherry

The bacteria transformed with pGEX2T-GST-pVCA-3Csite-SspB(micro)-mCherry-TEVsite-6×His were cultured overnight in LB broth supplemented with 100 µg/mL Ampicillin and 25 µg/mL Chloramphenicol (LB/Amp/Cam). Pre-culture was inoculated to LB/Amp/Cam and cultured at 37°C until OD_{600} reached around 0.5–0.6. After cooling the culture on ice, protein expression was induced by adding 300 µM IPTG and allowed to proceed for 24–26 hours at 18°C. The cells were resuspended with buffer V (50 mM HEPES-NaOH (pH 7.5), 150 mM NaCl, 10% glycerol, 14 mM b-mercaptoethanol, 1 mM EDTA, 1 mM PMSF, 100 µg/mL DNase, supplemented with cOmplete EDTA-free protease inhibitor cocktail) and lysed by microfluidizer. The lysate was centrifuged at 20,000×g at 4°C for 30 min to remove cell debris. To enhance resin binding, final 5 mM DTT was added to the lysate. The lysate was applied to glutathione sepharose equilibrated with buffer V [50 mM HEPES-NaOH (pH 7.5) 150 mM NaCl, 10% glycerol, 7 mM b-

mercaptoethanol, and 1 mM PMSF], and the protein was eluted with 20 mM glutathione in buffer V (pH was adjusted between 7.0–8.0 by NaOH). The elution was then purified by Ni-NTA and eluted with 50–500 mM imidazole. After concentrated by Amicon Ultra (10 kDa cutoff), the protein was further purified by Superdex 200 increase 10/300 GL column in buffer V and concentrated again by Amicon Ultra (10 kDa cutoff). The protein was snap-frozen in liquid nitrogen and stored at -80 °C.

mCherry-SspB-mDia1

The bacteria transformed with pET28-2×Strep-mCherry-SspB(micro)-mDia1(FH1-FH2-DAD) were cultured overnight in LB broth supplemented with 50 µg/mL Kanamycin and 25 µg/mL Chloramphenicol (LB/Kan/Cam). Pre-culture was inoculated to LB/Kan/Cam and cultured at 37°C until OD_{600} reached around 0.5–0.6. After cooling the culture on ice, protein expression was induced by adding 300 µM IPTG and allowed to proceed for 24 hours at 16°C. The cells were resuspended with buffer D [50 mM Tris-HCl (pH 7.5), 500 mM NaCl, 10% glycerol, 1 mM DTT, 1 mM EDTA, 1 mM PMSF, 100 µg/mL DNase, supplemented with cOmplete EDTA-free protease inhibitor cocktail] and lysed by microfluidizer. The lysate was centrifuged at 20,000×g at 4°C for 30 min to remove cell debris. The supernatant was applied to Strep-Tactin XT (IBA Lifesciences) equilibrated with buffer D1 (50 mM Tris-HCl (pH 7.5), 500 mM NaCl, 10% glycerol, 1 mM DTT, 1 mM EDTA, 1 mM PMSF) and the protein was eluted with 50 mM biotin in buffer D1. The elution was concentrated by Amicon Ultra (10 kDa cutoff) and dialysed against buffer D2 [25 mM HEPES-NaOH (pH 7.5), 150 mM NaCl, 7 mM b-mercaptoethanol, 10% glycerol]. The protein was further purified by Superdex 200 increase 10/300 GL column in buffer D2 and concentrated again by Amicon Ultra (10 kDa cutoff). The protein was snap-frozen in liquid nitrogen and stored at -80 °C.

Capping protein

The bacteria transformed with pET28-6×His-2×Strep-TEVsite-Capβ2(mouse)-Capα1(mouse) were cultured overnight in LB/Kan/Cam. Pre-culture was inoculated to LB/Kan/Cam and cultured at 37°C until OD_{600} reached around 0.7. Protein expression was induced by adding 300 µM IPTG and allowed to proceed for 24 hours at 18°C. The cells were re-suspended with 50 mM Tris-HCl (pH 7.5 at RT), 150 mM NaCl, 14 mM β-mercaptoethanol, 1 mM EDTA, 1 mM PMSF, 100 µg/mL DNase and lysed by microfluidizer. The lysate was centrifuged at 20,000×g at 4°C for 30 min to remove cell debris. The supernatant was applied to Strep-Tactin XT 4Flow (IBA Lifesciences) equilibrated with buffer C1 [50 mM Tris-HCl (pH 7.5 at RT), 150 mM NaCl, 7 mM β-mercaptoethanol] and the protein was eluted with 50 mM biotin in buffer C1. The elution was dialyzed against buffer C2 [25 mM Tris-HCl (pH 7.5 at RT), 150 mM NaCl, 7 mM β-mercaptoethanol]. 6×His-2×Strep tag was cleaved by 6×His-MBP-TEV protease (S219V) (purified in house) during the dialysis. The cleaved 6×His-2×Strep tag and TEV protease were removed

through Ni-NTA column. Flow through and wash fractions were dialyzed against buffer and concentrated by Amicon Ultra (10 kDa cutoff). The protein was snap-frozen in liquid nitrogen in buffer C2 and stored at -80 °C.

Pyrene-actin polymerization assay

For pyrene actin assay, actin was purified by size exclusion column. One milligram of actin (Cytoskeleton Inc. AKL99-B) was dissolved in 400 µL G-buffer [2 mM Tris-HCl (pH 7.5 at RT), 0.1 mM $CaCl_2$, 0.2 mM ATP, 0.5 mM DTT, 1 mM NaN_3] and dialyzed against the same buffer. After 3 days dialysis with daily buffer exchange, the actin was purified by Superdex 200 Increase 10/300 GL column (GE Healthcare) to separate monomer fraction from a fraction occasionally appear at larger size molecular size (smaller elution volume). The purified actin was stored at 4°C in a dialyzed manner against G-Buffer with twice a week buffer exchange.

Pyrene-actin polymerization assay was performed with FluoroMax 3 and Datamax software. Pyrene fluorescence and its kinetics were measured by 365 nm excitation (1 nm bandwidth) and 407 nm emission (5 nm bandwidth). The reaction was prepared by following the previously reported method (*127*), except that the reaction was 50 µL in quartz cuvettes (Hellma, 105-251-15-40).

GUV preparation by emulsion transfer

Lipid-in-oil solution was prepared as follows. Chloroform solutions of lipids were mixed in 5 mL glass vial, dried at 70°C with N_2 gas flow, and left in vacuum 3 hours to overnight. The amounts of lipids were typically 6.5 µmol (1.3 mM, 1 mg/mL at final concentration in oil) for 40 mol% POPS/60 mol% POPC mixture (MARCKS peptide anchoring) and 1.5 µmol (0.3 mM, 0.23 mg/mL at final concentration in oil) for 2 mol% Bendylguanine-conjugated lipid/98 mol% POPC and 100% POPC (SNAP-tag anchoring). was dissolved in 5 mL of oil mixture (90 volume% hexadecane, 10 volume% silicone oil) by heating at 80˚C for 1–2 hours, then brought to RT.

For iLID-SspB translocation experiments, inner solution contained 4 µM iLID-YFP-SNAP (or iLID-EYFP-MARCKS) and 1 µM mCherry-SspB(micro) in buffer (22.5 mM Tris-HCl (pH 7.5 at RT), 122.5 mM NaCl, 2 mM $MgCl_2$, 240 mM sucrose, 0.7 mM β-mercaptoethanol, and 3% glycerol). Outer solution was prepared by replacing protein fractions of inner solution with their buffers and sucrose with glucose.

For actin polymerization experiments, inner solution was prepared by mixing 10 µL of actin (10% Alexa 647 labelled) in G-buffer and 10 µL of other proteins solution similarly to pyrene actin polymerization assay. At the final concentration, inner solution typically contained 11.75 µM iLID-EYFP-SNAP, 1 µM GST-pVCA-SspB(micro)-mCherry, 1 µM mCherry-SspB(micro)-mDia1, 7.5 µM actin, 150 nM Arp2/3, 50 nM capping protein, 3 µM profilin, 2 µM cofilin, 1 µM creatine kinase in the buffer (5.9 mM Tris-HCl (pH 7.5 at RT), 1.3 mM HEPES-NaOH (pH 7.5 at RT), 7.7 mM Imidazole (pH 8.0 at RT), 27 µM KH_2PO_4, 74 µM Na_2HPO_4, 39 mM KCl, 33 mM NaCl, 0.8

mM $MgCl_2$, 43 µM $CaCl_2$, 1.1 mM EGTA, 1.2 mM β-mercaptoethanol, 0.21 mM DTT, 0.43 mM NaN_3, 1 mM ATP, 25 mM creatine phosphate, 240 mM sucrose and 2.8% glycerol). Outer solution was prepared by replacing protein fractions of inner solution with their buffers and sucrose with glucose. Protein and buffer conditions are summarized in Supplementary table 1.

GUVs were prepared as previously reported (*55*, *128*). Briefly, oil-buffer interface was created by layering 250 µL lipid-in-oil solution on top of 250 µL outer buffer in 1.5 mL tube. Water-in-oil emulsion was made by vigorously pipetting 20 µL of inner solution in 250 µL of lipid-in-oil solution and gently added to the top of the oil-buffer layers. The emulsions were transferred through the oil-buffer interface by centrifugation at 2500×g for 2 min at RT. GUVs were collected by pipetting.

Image acquisition and analysis

For imaging GUVs, 8-well glass chamber slides (ThermoFisher Scientific, 154534) were pretreated with 10 mg/mL BSA in PBS for 10 minutes and washed with MilliQ water twice. LSM780 confocal microscope (Zeiss) equipped with Plan-Aprochromat 63X/1.40na oil immersion DIC objective lens (Zeiss 420782-9900) was used for imaging and light stimulation of GUVs. YFP, mCherry, and Alexa Fluor 647 were imaged with 514, 561, and 633 nm excitation lasers, respectively. Blue light illumination for iLID stimulation was performed by using bleaching function with 458 nm laser at intensity 1.0–5.0%, scan speed 6 (pixel dwell time = 6.3 µsec). Main beam splitters MBS458/561, MBS 488/561/633, and MBS 458/514 were used for 458 and 561, 633, and 514 nm excitation, respectively. The imaging was performed at room temperature. Data were analyzed by Fiji software (*129*).

Live cell CID experiments

DNA constructs: Four plasmids were used which encoded Lyn-CFP-FRB (*130*), YFP-FKBP (*130*), YFP-FKBP-Tiam1 (*124*), YFP-FKBP-pVCA, and YFP-FKBP-mDia1.

Cell culture: HEK293T cells (ATCC) were cultured in DMEM (Corning, 10-013-CV) supplemented with 10% fetal bovine serum (Corning, 35-010-CV) and 1% penicillin-streptomycin (ThermoFisher, 15140163).

Transient transfection: HEK293T cells were seeded at a density of 9,000-12,000 cells in an 8-well chamber slide. A solution of 0.3 µg of DNA, 1 µL of FuGENE HD, and 30 µL of Opti-MEM per well was added for transfection. FRB:FKBP pairs were cotransfected in a 1:1 or 1:2 ratio. Cells were incubated at 37°C with 5% CO_2 and 95% humidity for 24–48 h before imaging.

Microscopes and imaging: Live cell imaging of actin NPF recruitment to the cell membrane was performed using an Eclipse Ti inverted fluorescence microscope (Nikon) with a 100x Oil objective lens and Andor Zyla 4.2 plus sCMOS camera, or with a 60x Oil, TIRF 60x Oil, or TIRF 100x Oil objective lens and ORCA-Fusion Digital CMOS camera. Images were captured every 1 min for 30-120 min, where within 5 min of starting, 0.1 µM rapamycin was added. Nikon

microscopes were driven by NIS-Elements software (Nikon). All live cell imaging was performed at 37 °C with 5% CO_2 and humidity control by a stage top incubator. Image processing and analysis were performed by Fiji software.

Data analysis: Per transfection sample, each cell from the image set was counted between three categories. The categories were no change, lamellipodia, and filipodia. Cells with lamellipodia or filipodia pre-rapamycin were not counted unless new membrane protrusions formed after rapamycin addition. If the cell under observation did not produce any new lamellipodia or filipodia after addition of rapamycin, then it was counted as no change. Only healthy cells fully in the plane of view with clear expression of both FRB and FKBP constructs were counted. If there was any doubt in the phenotype of the cell, then it was not included in the count.

Statistics

1. The cell counts for each category were summed across all experiments, and this sum was divided by the total number of cells to get a percentage of cells belonging to each category when a certain actin NPF was recruited to the membrane.

2. For each image set collected from a transfection sample, the categorized cell counts were divided by the total cell count to get percentages. For each actin NPF, the percentages from all transfection samples were averaged. These averages were analyzed by two-tailed Student's t-test assuming equal variance (checked with F-test) in order to establish the significance of lamellipodia or filopodia detection between transfection samples.

Acknowledgement

We thank Yubin Zhou for TEV protease plasmid; Masato Kanemaki for pET28-2×Strep-tag plasmid; Miho Iijima for pGEX-2T plasmid; Bin Wu for Phage-ubc-nls-ha-tdMCP-SNAP plasmid; Roberto Dominguez for pCold-mDia1 plasmid, Saki Takayanagi for constructing GST-pVCA-FKBP-EYFP plasmid. We also thank Yusuke Sato, Taro Toyota, Pushpendra Singh, Tetsuya Kotani, Takeya Masubuchi for technical advice on the experiments. We appreciate Erin D. Goley for technical support of pyrene assay and insightful comments on actin preparation. We also appreciate Julie Plastino and Cecile Sykes for pET3d-Capβ2(mouse)-Capα1(mouse) plasmid and insightful advice on protein purification. Our appreciation extends to Pablo A. Iglesias for fruitful discussion. We thank our lab members, including Allen Kim, Abhijit Deb Roy, Helen D. Wu, Yuta Nihongaki for constructive discussion. We thank Kyoko Chiba for technical support on protein purification. We also thank Robert DeRose for proofreading the manuscript and experimental support. FRIS CoRE (a shared research environment in Tohoku University) is also acknowledged. This study was supported by the PRESTO program of the Japan Science and Technology Agency (JPMJPR12A5 to TI, JPMJPR20KA to HTM), National Institute of Health (5R01GM123130, R01GM136858, R35GM149329 to TI, and R35GM128786 to BC), and the

National Science Foundation (000819255 to TI, JL, BC). TI was also supported by Nitto Denko Corp. HTM was supported by Postdoctoral Fellowships from the Japan Society for the Promotion of Science. SR was supported by the National Science Foundation and the Japan Society for the Promotion of Science (JSPS) East Asia and Pacific Summer Institutes and Johns Hopkins Lucille Elizabeth Hay graduate fellowships.

Author contributions

HTM, SR, and TI conceived the project. HTM performed most of the experiments and analyzed the data with contributions from SR, HN, BC, SM, SMN and TI. SR established GUV preparation method. WR performed in-cell CID experiment and analyzed the data. DN, DAK, and BC provided cytoskeleton proteins. TM provided benzylguanine-conjugated lipid. HTM wrote the manuscript in consultation with TI. HTM, SR, and TI edited the manuscript. All the authors contributed to the final version of the manuscript.

Figure Legends

Fig. 1. Reversible and asymmetric control of protein localization with iLID-SspB within GUVs. (A) Schematic representation of iLID-SspB reaction with global light stimulation. iLID was tethered on the membrane via the interaction between SNAP-tag and bendylguanine-conjugated lipids. Upon blue light illumination, Jα helix of iLID extends to expose the binding site for SspB, whereas in the dark, iLID reverses to its closed state and releases SspB. (B) Representative images of iLID-YFP-SNAP and mCherry-SspB. Scale bar, 10 µm. Blue bar indicates the period of blue light illumination. (C) Time course of membrane/lumen ratio of mCherry-SspB signal (n=5). Error bars indicate standard deviation. Blue area indicates the period of blue light stimulation. Triangles indicate timepoints represented in (B). (D) Schematic representation of iLID-SspB reaction with local light stimulation. (E) Representative images of mCherry-SspB. Scale bar, 10 µm. Yellow box indicates the area of blue light illumination. (F) Membrane/lumen ratio of mCherry-SspB for the representative image shown. The distance is measured from the center of blue light illumination along the perimeter of the GUV. (G) Representative image and kymograph of repetitive and reversible SspB translocation. Kymograph shows membrane signal of mCherry-SspB.

Fig. 2. Reversible light control of actin cytoskeleton within GUVs. (A) Bulk pyrene actin polymerization assay with 1 µM actin (5% pyrene labeled), 10 nM Arp2/3, and 100 nM NPFs. (-NPF) represents actin and Arp2/3 only condition. (B) Schematic representation of light inducible actin polymerization. Translocation of pVCA-SspB-mCherry increases local concentration of

pVCA on the membrane and enhances actin polymerization. (C) Representative images of pVCA-SspB-mCherry and Alexa 647 actin. Blue bar indicates the period of blue light illumination. (D), (E) Time course of membrane/lumen ratio of mCherry and Alexa 647 actin. +: full set of components (n=4). -Light: no blue light stimulation (n=3). -pVCA: pVCA-SspB-mCherry was replaced with mCherry-SspB (n=4). -Arp2/3: Arp2/3 was omitted (n=4). Error bars indicate 95% CI. Triangles indicate timepoints represented in (C). (F) Representative images of reversible actin polymerization. Blue bars indicate the period of blue light illumination. (G) Time course of membrane/lumen ratio of pVCA-SspB-mCherry and Alexa 647-labeled actin in (F). Triangles indicate timepoints represented in (F).

Fig. 3. Asymmetric light control of actin cytoskeleton within GUVs. (A) Schematic representation of iLID-SspB reaction with local light stimulation. (B, D) Representative images of light inducible asymmetric actin polymerization. Yellow boxes indicate the area of blue light illumination. (C, E) Kymograph of membrane pVCA-SspB and actin signals. Blue bars indicate the period of blue light illumination. Triangles indicate timepoints represented in (B, D).

Fig. 4. mDia1-mediated actin polymerization drives protrusive motility of GUVs. (A) Schematic representation of light inducible membrane protrusion driven by pVCA and mDia1-mediated actin polymerization. (B) Representative images of pVCA-mDia1-mediated movement of GUVs. Yellow boxes indicate the area of blue light stimulation. Dotted line shows the initial position of the GUV. (C) Representative images of iLID-EYFP-SNAP showing the increase in adhesive area and vesicle deformation into dome-like shape. Bottom plane indicates the confocal plane right above the bottom substrate. Side view is reconstituted from z-stack. Dotted line shows the adhesive area of the previous images. (D) Color-coded boundaries of GUVs. The data correspond as follows. Left: Fig. 4B. Middle: Fig. S16A. Right: Fig. S16B. (E, F) Kymographs of membrane signal of mCherry and actin Alexa-647 and membrane protrusions. Triangles in (E) indicate the timepoints represented in (B, C). Data of (E) and (F) corresponds to Fig. 4 (B) and Fig. S16A, respectively. (G) Distance the front (illuminated) side of GUV membrane moved forward. pVCA+mDia1 (1 µM GST-pVCA-SspB-mCherry + 1 µM mCherry-SspB-mDia1, n=14 vesicles), mDia1 (1 µM mCherry-SspB-mDia1, n=12 vesicles), pVCA (1 µM GST-pVCA-SspB-mCherry, n=12 vesicles). Error bars indicate standard error of the mean (SEM). (H) DMSO (n=9 vesicles), 30 µM LatA (Latrunculin A) (n=10 vesicles). DMSO, ΔDAD: mCherry-SspB-mDia1 (FH1-FH2-DAD) was replaced with mCherry-SspB-mDia1(FH1-FH2) (n=13 vesicles). 30 µM SMIFH2 (n=6 vesicles). Error bars indicate standard error of the mean (SEM). (I) A GUV deformed into dome-like shape after movement. Upper images: before light stimulation. Lower images: after light stimulation. The data corresponds to Fig. S16C.

Fig. S1. Proteins purified in this study. (A) SDS-PAGE results of purified proteins. Blue: Coomassie brilliant blue staining. Gray: SYPRO Ruby staining. Most mCherry-tagged proteins show two extra bands due to a known chromophore cleavage reaction during the boiling process (*131*, *132*). (B) Domain structures of NPFs used in this study.

Fig. S2. Optimization of membrane anchoring of iLID. (A),(D),(G),(I): Schematic representations of membrane anchoring of iLID. (B),(C),(E),(F),(H),(J): Confocal images of iLID variants and mCherry-SspB. (B) His-tag Ni-NTA pair caused non-specific membrane recruitment of SspB. This is possibly caused by the presence of 2×Strep-iLID-YFP-6×His because mCherry-SspB itself did not show non-specific binding to the membrane of 5%Ni-NTA DGS/95%POPC (C). (E),(F) MARCKS-ED peptide requires high percentage of PS and PEGylated-lipids to reduce non-specific binding of SspB. (H) Biotin-StrepTactin-Streptag also caused non-specific membrane binding of SspB. (J) The data correspond with Fig. 1B.

Fig. S3. Asymmetric control of protein localization with iLID-SspB within GUVs. (A) Time course of membrane/lumen ratio of mCherry-SspB signal in the illuminated area (n=5). Error bars indicate 95% CI. Blue area indicates the time window of blue light stimulation. The data corresponds to Fig. 1E and F. (B, C) Confocal images and time course of membrane/lumen ratio of mCherry-SspB signal responding to repetitive local light illuminations. The data corresponds to Fig. 1G.

Fig. S4. Optimization of ActA-SspB. (A) Pyrene actin polymerization assay. The reaction was performed with 1 µM actin (5% pyrene labeled), 10 nM Arp2/3, and 100 nM ActA variants or GST-VCA. (B) Fluorescence intensity/time in 0–6 min of (A) was plotted as bar chart. (C–E) Light inducible local membrane recruitment of ActA (C) Confocal images of ActA translocation. Yellow boxes indicate the area of blue light illumination. (D) Time course of membrane/lumen ratio of ActA-SspB variants (n≥5 for each variant). Error bars indicate SEM. Blue bar indicates the time window of blue light stimulation. (E) Average membrane/lumen ratio of mCherry signal. In each condition, left and right bars indicate before and after light stimulation, respectively. The numbers on the bar chart indicate the fold change after stimulation.

Fig. S5. Light inducible actin polymerization with global ActA membrane recruitment. iLID-EYFP-MARCKS (5 µM), ActA-SspBnano-mCherry (2 µM), actin (1.5 µM, 10% Alexa-647 labeled), and Arp2/3 (150 nM) were encapsulated in GUVs containing 60 mol% POPC/40 mol% POPS. Blue light was applied to the entire GUV. (A) Representative images of ActA(1–183)-SspB(nano)-mCherry and actin Alexa-647. All components (n=4): w/o ActA: ActA(1–183)-SspB(nano)-mCherry was replaced with mCherry-SspB(micro) (n=3), w/o Arp2/3: Arp2/3 was omitted (n=3). No Light: no blue light stimulation (n=3). (B, C) Time course of membrane/lumen ratio of

mCherry and actin Alexa 647. (D) Bar chart of membrane/lumen ratio of actin Alexa 647 before (0 min) and after (40 min) light stimulation. Error bars indicate SEM.

Fig. S6. Asymmetric ActA membrane recruitment fails to induce directed actin polarization toward local light illumination. iLID-EYFP-MARCKS (5 µM), ActA-SspBnano-mCherry (2 µM), actin (1.5 µM, 10% Alexa-647 labeled), and Arp2/3 (150 nM), 1 mM ATP were encapsulated in GUVs containing 60 mol% POPC/40 mol% POPS. Yellow boxes indicate the area of blue light illumination. Although ActA creates asymmetric distribution, actin patches randomly distributed due to the diffusion on the membrane.

Fig. S7. Global ActA membrane recruitment fails to induce actin polymerization on the membrane in the presence of profilin, cofilin, and capping protein. 15 µM iLID-YFP-MARCKS, 5 µM ActA(1-183)-SspB(nano)-mCherry, 7.5 µM actin (10% Alexa 647 labeled), 150 nM Arp2/3, 3 µM profilin, cofilin, and capping protein were encapsulated in GUVs containing 60 mol% POPC/40 mol% POPS. Blue bars indicate the period of blue light illumination.

Fig. S8. Pyrene actin polymerization assay. (A, B) The reactions were performed with 2 µM actin (5% pyrene labeled), 10 nM Arp2/3, and 100 nM NPFs at RT. (-) represents actin and Arp2/3 only condition. (C) The reactions were performed with 2 µM actin (5% pyrene labeled) with the indicated factors.

Fig. S9. Light control of actin cytoskeleton with pVCA-SspB-mCherry. The data correspond to Fig. 2C–E. (+) condition contains 15 µM iLID-YFP-MARCKS, 4.2 µM pVCA-SspB(nano)-mCherry, 7.5 µM actin (10% Alexa 647 labelled), 150 nM Arp2/3, 100 nM capping protein, 3 µM profilin, 4 µM cofilin, and 1 mM ATP. In (-light) and (-Arp2/3) conditions, blue light illumination or Arp2/3 was omitted from (+) condition, respectively. In (-pVCA) condition, pVCA-SspB(nano)-mCherry was replaced with mCherry-SspB(micro).

Fig. S10. Representative images of reversible actin polymerization. Confocal images and time course of membrane/lumen ratio of pVCA-SspB-mCherry and Alexa 647-labeld actin. Blue bars on images and blue regions in graphs indicate timepoints with blue light illumination. This figure corresponds with Fig. 2F, G.

Fig. S11. Asymmetric actin polymerization induced by pVCA. (A, B) Confocal images of local pVCA recruitment and actin polymerization. Yellow boxes indicate areas of blue light illumination. (A) The data corresponds to Fig. 3B and C. In (B), Vesicle movement toward light

stimulation was observed. Gray scaled images were created by averaging pVCA and actin images. Dotted circles indicate positions of vesicles in the images of one above.

Fig. S12. Quantitative analysis of mDia1-induced filopodia formation in Cos7 cells. (A) Schematic representation of chemically-inducible mDia1 translocation and membrane protrusions. (B, C) Confocal images of plasma membrane recruitment of mDia1 and subsequent filopodia formation. Cos7 cells were transfected with Lyn-ECFP-FRB, Lifeact-mCherry, and either of YFP-FKBP or YFP-FKBP-mDia1. At time 0, 100 nM rapamycin was added. Green: YFP-FKBP or YFP-FKBP-mDia1. Magenta: Lifeact-mCherry. (B) YFP-FKBP control. (C) YFP-FKBP-mDia1. (D) Zoomed-up view of filopodia extension. Images were acquired every 1.5 minutes. The bottom is merged image. (E) Quantification of mDia1-induced filopodia. Number of filopodia whose length is longer than 15 µm was counted. P-values: ****: < 0.0001. Wilcoxon rank sum test. YF (YFP-FKBP): n=36 cells. YF-mDia1 (YFP-FKBP-mDia1): n=33 cells. (F–H) Quantification of the phenotypes observed after plasma membrane translocation of mDia1, pVCA, Tiam1 (Rac1 GEF), and control protein YFP-FKBP.

Fig. S13. mDia1-mediated GUV movement and the comparison between mDia1 and pVCA + mDia1 system. (A) Representative images of mDia1-mediated GUV movement. Yellow boxes indicate the area of blue light stimulation. Dotted lines indicate the initial position of the GUV. (B, C) Time course of the distance the front (illuminated) side of GUV membrane moved forward. Each line represents each GUVs. Insets show the initial response. (D, E) Quantification of the initial velocity and the distance the front side of GUV membrane moved forward. P values of Steel-Dwass test (two sided) are indicated. pVCA + mDia1: n=22 vesicles. mDia1: n=11 vesicles. pVCA: n=12 vesicles. Box whisker plots represent median, 1st, 3rd quartiles and 1.5×inter-quartile range.

Fig. S14. Local protrusions in pVCA + mDia1 GUVs. Representative images of local protrusions seen in pVCA + mDia1 GUVs. Yellow boxes indicate the area of blue light stimulation. Dotted lines indicate the initial position of the GUV. White arrows indicate where local protrusions arose.

Fig. S15. Lack of vesicle movement and shape change with mCherry-SspB. With pVCA-SspB-mCherry and mCherry-SspB-mDia1 being replaced with mCherry-SspB, GUVs neither moved nor changed their shape after blue light illumination. (A) Time course of the distance the front (illuminated) side of GUV membrane moved forward. pVCA + mDia1 GUVs: n=6 vesicle. SspB GUVs: n=4 vesicles. Error bars indicate SEM. (B) 3D reconstitution of iLID-YFP-SNAP images before and after blue light illumination.

Fig. S16. Representative images of pVCA-mDia1-mediated movement of GUVs. (A, B) Representative images of pVCA-mDia1-mediated movement of GUVs. Yellow boxes indicate the area of blue light stimulation. Dotted lines indicate the initial position of the GUV. White arrows indicate where local protrusions arose. (C) Distance the front side of GUV membrane moved forward. Data was quantified from the images of (B). Blue areas indicate the periods of blue light stimulation.

References

1. M. Miyata, R. C. Robinson, T. Q. P. Uyeda, Y. Fukumori, S. ichi Fukushima, S. Haruta, M. Homma, K. Inaba, M. Ito, C. Kaito, K. Kato, T. Kenri, Y. Kinosita, S. Kojima, T. Minamino, H. Mori, S. Nakamura, D. Nakane, K. Nakayama, M. Nishiyama, S. Shibata, K. Shimabukuro, M. Tamakoshi, A. Taoka, Y. Tashiro, I. Tulum, H. Wada, K. ichi Wakabayashi, Tree of motility – A proposed history of motility systems in the tree of life. *Genes to Cells* **25**, 6–21 (2020).

2. K. Y. Wan, G. Jékely, Origins of eukaryotic excitability. *Phil. Trans. R. Soc. B* **376**, 20190758 (2021).

3. T. Froese, N. Virgo, T. Ikegami, Motility at the Origin of Life: Its Characterization and a Model. *Artificial Life* **20**, 55–76 (2014).

4. P. N. Devreotes, S. Bhattacharya, M. Edwards, P. A. Iglesias, T. Lampert, Y. Miao, Excitable Signal Transduction Networks in Directed Cell Migration. *Annu. Rev. Cell Dev. Biol.* **33**, 103–125 (2017).

5. L. K. Fritz-Laylin, The evolution of animal cell motility. *Current Biology* **30**, R477–R482 (2020).

6. S. SenGupta, C. A. Parent, J. E. Bear, The principles of directed cell migration. *Nat Rev Mol Cell Biol* **22**, 529–547 (2021).

7. S. B. Carter., Effects of Cytochalasins on Mammalian Cells. Nature 213, 261-264 (1967).

8. T. D. Pollard, S. Ito, CYTOPLASMIC FILAMENTS OF *AMOEBA PROTEUS*. *The Journal of Cell Biology* **46**, 267–289 (1970).

9. J. V. Small, G. Isenberg, J. E. Celis, Polarity of actin at the leading edge of cultured cells. *Nature* **272**, 638–639 (1978).

10. L. G. Tilney, S. Inoué, Acrosomal reaction of Thyone sperm. II. The kinetics and possible mechanism of acrosomal process elongation. *J Cell Biol* **93**, 820–827 (1982).

11. J. A. Theriot, The Polymerization Motor. *Traffic* **1**, 19–28 (2000).

12. T. D. Pollard, Landmarks in the discovery of a role for actin in cell locomotion. *Molecular Biology of the Cell*, 4 (2022).

13. P. Lappalainen, T. Kotila, A. Jégou, G. Romet-Lemonne, Biochemical and mechanical regulation of actin dynamics. *Nat Rev Mol Cell Biol*, doi: 10.1038/s41580-022-00508-4 (2022).

14. P. Friedl, K. Wolf, Plasticity of cell migration: a multiscale tuning model. *Journal of Cell Biology* **188**, 11–19 (2010).

15. T. Lämmermann, M. Sixt, Mechanical modes of 'amoeboid' cell migration. *Current Opinion in Cell Biology* **21**, 636–644 (2009).

16. M. Garrido-Casado, G. Asensio-Juárez, M. Vicente-Manzanares, Nonmuscle Myosin II Regulation Directs Its Multiple Roles in Cell Migration and Division. *Annu Rev Cell Dev Biol* **37**, 285–310 (2021).

17. D. Knecht, W. Loomis, Antisense RNA inactivation of myosin heavy chain gene expression in Dictyostelium discoideum. *Science* **236**, 1081–1086 (1987).

18. A. De Lozanne, J. A. Spudich, Disruption of the Dictyostelium myosin heavy chain gene by homologous recombination. *Science* **236**, 1086–1091 (1987).

19. A. B. Verkhovsky, T. M. Svitkina, G. G. Borisy, Self-polarization and directional motility of cytoplasm. *Current Biology* **9**, 11-S1 (1999).

20. R. J. Eddy, L. M. Pierini, F. Matsumura, F. R. Maxfield, Ca2+-dependent myosin II activation is required for uropod retraction during neutrophil migration. *J Cell Sci* **113 (Pt 7)**, 1287–1298 (2000).

21. T. Lämmermann, B. L. Bader, S. J. Monkley, T. Worbs, R. Wedlich-Söldner, K. Hirsch, M. Keller, R. Förster, D. R. Critchley, R. Fässler, M. Sixt, Rapid leukocyte migration by integrin-independent flowing and squeezing. *Nature* **453**, 51–55 (2008).

22. A. Reversat, F. Gaertner, J. Merrin, J. Stopp, S. Tasciyan, J. Aguilera, I. de Vries, R. Hauschild, M. Hons, M. Piel, A. Callan-Jones, R. Voituriez, M. Sixt, Cellular locomotion using environmental topography. *Nature* **582**, 582–585 (2020).

23. Y. I. Wu, D. Frey, O. I. Lungu, A. Jaehrig, I. Schlichting, B. Kuhlman, K. M. Hahn, A genetically encoded photoactivatable Rac controls the motility of living cells. *Nature* **461**, 104–108 (2009).

24. B. Lin, W. R. Holmes, C. J. Wang, T. Ueno, A. Harwell, L. Edelstein-Keshet, T. Inoue, A. Levchenko, Synthetic spatially graded Rac activation drives cell polarization and movement. *Proceedings of the National Academy of Sciences of the United States of America* **109** (2012).

25. S. Nanda, A. Calderon, A. Sachan, T.-T. Duong, J. Koch, X. Xin, D. Solouk-Stahlberg, Y.-W. Wu, P. Nalbant, L. Dehmelt, Rho GTPase activity crosstalk mediated by Arhgef11 and Arhgef12 coordinates cell protrusion-retraction cycles. *Nat Commun* **14**, 8356 (2023).

26. L. A. Cameron, M. J. Footer, A. Van Oudenaarden, J. A. Theriot, Motility of ActA protein-coated microspheres driven by actin polymerization. *Proceedings of the National Academy of Sciences of the United States of America* **96**, 4908–4913 (1999).

27. T. P. Loisel, R. Boujemaa, D. Pantaloni, M. Carlier, Reconstitution of actin-based motility of Listeria and Shigella using pure proteins. **401**, 613–616 (1999).

28. A. Bernheim-Groswasser, S. Wiesner, R. M. Golsteyn, M.-F. Carlier, C. Sykes, The dynamics of actin-based motility depend on surface parameters. *Nature* **417**, 308–311 (2002).

29. A. Mogilner, G. Oster, Force generation by actin polymerization II: The elastic ratchet and tethered filaments. *Biophysical Journal* **84**, 1591–1605 (2003).

30. S. Wiesner, E. Helfer, D. Didry, G. Ducouret, F. Lafuma, M. F. Carlier, D. Pantaloni, A biomimetic motility assay provides insight into the mechanism of actin-based motility. *Journal of Cell Biology* **160**, 387–398 (2003).

31. S. Romero, C. Le Clainche, D. Didry, C. Egile, D. Pantaloni, M. F. Carlier, Formin is a processive motor that requires profilin to accelerate actin assembly and associated ATP hydrolysis. *Cell* **119**, 419–429 (2004).

32. C. Co, D. T. Wong, S. Gierke, V. Chang, J. Taunton, Mechanism of Actin Network Attachment to Moving Membranes: Barbed End Capture by N-WASP WH2 Domains. *Cell* **128**, 901–913 (2007).

33. O. Akin, R. D. Mullins, Capping Protein Increases the Rate of Actin-BasedMotility by Promoting Filament Nucleation by the Arp2/3 Complex. *Cell* **133**, 841–851 (2008).

34. J. Prost, J.-F. Joanny, P. Lenz, C. Sykes, "The Physics Of Listeria Propulsion" in *Cell Motility* (Springer New York, New York, NY, 2008; https://doi.org/10.1007/978-0-387-73050-9_1), pp. 1–30.

35. P. Bieling, S. D. Hansen, O. Akin, T.-D. Li, C. C. Hayden, D. A. Fletcher, R. D. Mullins, WH2 and proline-rich domains of WASP-family proteins collaborate to accelerate actin filament elongation. *EMBO J* **37**, 102–121 (2018).

36. S. Razavi, T. Inoue, "Chapter 22 - Reconstitution of membrane symmetry breaking" in *Plasma Membrane Shaping*, S. Suetsugu, Ed. (Academic Press, 2023; https://www.sciencedirect.com/science/article/pii/B9780323899116000273), pp. 333–353.

37. R. Lopes Dos Santos, C. Campillo, Studying actin-induced cell shape changes using Giant Unilamellar Vesicles and reconstituted actin networks. *Biochemical Society Transactions* **50**, 1527–1539 (2022).

38. F. C. Keber, E. Loiseau, T. Sanchez, S. J. DeCamp, L. Giomi, M. J. Bowick, M. C. Marchetti, Z. Dogic, A. R. Bausch, Topology and dynamics of active nematic vesicles. *Science* **345**, 1135–1139 (2014).

39. Y. Sato, Y. Hiratsuka, I. Kawamata, S. Murata, S. M. Nomura, Micrometer-sized molecular robot changes its shape in response to signal molecules. *Science Robotics* **2**, eaal3735 (2017).

40. K. Gavriljuk, B. Scocozza, F. Ghasemalizadeh, H. Seidel, A. P. Nandan, M. Campos-Medina, M. Schmick, A. Koseska, P. I. H. Bastiaens, A self-organized synthetic morphogenic liposome responds with shape changes to local light cues. *Nature Communications* **12**, 1548 (2021).

41. J. D. Cortese, B. Schwab, C. Frieden, E. L. Elson, Actin polymerization induces a shape change in actin-containing vesicles. *Proceedings of the National Academy of Sciences of the United States of America* **86**, 5773–5777 (1989).

42. H. Miyata, H. Hotani, Morphological changes in liposomes caused by polymerization of encapsulated actin and spontaneous formation of actin bundles. *Proceedings of the National Academy of Sciences of the United States of America* **89**, 11547–11551 (1992).

43. H. Miyata, S. Nishiyama, K. -i. Akashi, K. Kinosita, Protrusive growth from giant liposomes driven by actin polymerization. *Proceedings of the National Academy of Sciences* **96**, 2048–2053 (1999).

44. M. Honda, K. Takiguchi, S. Ishikawa, H. Hotani, Morphogenesis of liposomes encapsulating actin depends on the type of actin-crosslinking. *Journal of Molecular Biology* **287**, 293–300 (1999).

45. L. L. Pontani, J. Van Der Gucht, G. Salbreux, J. Heuvingh, J. F. Joanny, C. Sykes, Reconstitution of an actin cortex inside a liposome. *Biophysical Journal* **96**, 192–198 (2009).

46. K. Dürre, F. C. Keber, P. Bleicher, F. Brauns, C. J. Cyron, J. Faix, A. R. Bausch, Capping protein-controlled actin polymerization shapes lipid membranes. *Nature Communications*, doi: 10.1038/s41467-018-03918-1 (2018).

47. Y. Bashirzadeh, S. A. Redford, C. Lorpaiboon, A. Groaz, H. Moghimianavval, T. Litschel, P. Schwille, G. M. Hocky, A. R. Dinner, A. P. Liu, Actin crosslinker competition and sorting drive emergent GUV size-dependent actin network architecture. *Commun Biol* **4**, 1136 (2021).

48. N. H. Wubshet, Y. Bashirzadeh, A. P. Liu, Fascin-induced actin protrusions are suppressed by dendritic networks in giant unilamellar vesicles. *MBoC* **32**, 1634–1640 (2021).

49. T. Litschel, C. F. Kelley, D. Holz, M. Adeli Koudehi, S. K. Vogel, L. Burbaum, N. Mizuno, D. Vavylonis, P. Schwille, Reconstitution of contractile actomyosin rings in vesicles. *Nature Communications* **12**, 2254 (2021).

50. R. Sakamoto, M. P. Murrell, Composite branched and linear F-actin maximize myosin-induced membrane shape changes in a biomimetic cell model. *Commun Biol* **7**, 1–12 (2024).

51. R. Sakamoto, D. S. Banerjee, V. Yadav, S. Chen, M. L. Gardel, C. Sykes, S. Banerjee, M. P. Murrell, Membrane tension induces F-actin reorganization and flow in a biomimetic model cortex. *Commun Biol* **6**, 325 (2023).

52. K. Y. Lee, S. J. Park, K. A. Lee, S. H. Kim, H. Kim, Y. Meroz, L. Mahadevan, K. H. Jung, T. K. Ahn, K. K. Parker, K. Shin, Photosynthetic artificial organelles sustain and control ATP-dependent reactions in a protocellular system. *Nature Biotechnology* **36**, 530–535 (2018).

53. S. Tanaka, K. Takiguchi, M. Hayashi, Repetitive stretching of giant liposomes utilizing the nematic alignment of confined actin. *Communications Physics* **1** (2018).

54. A. Fink, C. R. Doll, A. Yagüe Relimpio, Y. Dreher, J. P. Spatz, K. Göpfrich, E. A. Cavalcanti-Adam, Extracellular Cues Govern Shape and Cytoskeletal Organization in Giant Unilamellar Lipid Vesicles. *ACS Synth. Biol.*, acssynbio.2c00516 (2023).

55. S. Razavi, F. Wong, B. Abubaker-Sharif, H. T. Matsubayashi, H. Nakamura, N. T. H. Nguyen, D. N. Robinson, B. Chen, P. A. Iglesias, T. Inoue, Synthetic control of actin polymerization and symmetry breaking in active protocells. *Sci Adv* **10**, eadk9731 (2024).

56. K. Zhang, B. Cui, Optogenetic control of intracellular signaling pathways. *Trends in Biotechnology* **33**, 92–100 (2015).

57. A. Pudasaini, K. K. El-Arab, B. D. Zoltowski, LOV-based optogenetic devices: Light-driven modules to impart photoregulated control of cellular signaling. *Frontiers in Molecular Biosciences* **2**, 1–15 (2015).

58. J. Niu, M. Ben Johny, I. E. Dick, T. Inoue, Following Optogenetic Dimerizers and Quantitative Prospects. *Biophysical Journal* **111**, 1132–1140 (2016).

59. G. Guntas, R. A. Hallett, S. P. Zimmerman, T. Williams, H. Yumerefendi, J. E. Bear, B. Kuhlman, Engineering an improved light-induced dimer (iLID) for controlling the localization and activity of signaling proteins. *Proceedings of the National Academy of Sciences of the United States of America* **112**, 112–117 (2015).

60. A. Uyeda, T. Watanabe, T. Hohsaka, T. Matsuura, Different protein localizations on the inner and outer leaflet of cell-sized liposomes using cell-free protein synthesis. *Synthetic Biology* **3**, ysy007 (2018).

61. A. K. Rudd, J. M. Valls Cuevas, N. K. Devaraj, SNAP-Tag-Reactive Lipid Anchors Enable Targeted and Spatiotemporally Controlled Localization of Proteins to Phospholipid Membranes. *J. Am. Chem. Soc.* **137**, 4884–4887 (2015).

62. D. Scherfeld, N. Kahya, P. Schwille, Lipid dynamics and domain formation in model membranes composed of ternary mixtures of unsaturated and saturated phosphatidylcholines and cholesterol. *Biophysical journal* **85**, 3758–3768 (2003).

63. F. A. Thomas, I. Visco, Z. Petrášek, F. Heinemann, P. Schwille, Diffusion coefficients and dissociation constants of enhanced green fluorescent protein binding to free standing membranes. *Data in Brief* **5**, 537–541 (2015).

64. M. Frick, K. Schmidt, B. J. Nichols, Modulation of Lateral Diffusion in the Plasma Membrane by Protein Density. *Current Biology* **17**, 462–467 (2007).

65. R. D. Mullins, P. Bieling, D. A. Fletcher, From solution to surface to filament: actin flux into branched networks. *Biophys Rev* **10**, 1537–1551 (2018).

66. L. B. Case, X. Zhang, J. A. Ditlev, M. K. Rosen, Stoichiometry controls activity of phase-separated clusters of actin signaling proteins. *Science* **363**, 1093–1097 (2019).

67. H. Miki, K. Miura, T. Takenawa, N-WASP, a novel actin-depolymerizing protein, regulates the cortical cytoskeletal rearrangement in a PIP2-dependent manner downstream of tyrosine kinases. *The EMBO Journal* **15**, 5326–5335 (1996).

68. R. Rohatgi, L. Ma, H. Miki, M. Lopez, T. Kirchhausen, T. Takenawa, M. W. Kirschner, The Interaction between N-WASP and the Arp2/3 Complex Links Cdc42-Dependent Signals to Actin Assembly. *Cell* **97**, 221–231 (1999).

69. O. D. Weiner, G. Servant, M. D. Welch, T. J. Mitchison, J. W. Sedat, H. R. Bourne, Spatial control of actin polymerization during neutrophil chemotaxis. *Nature Cell Biology* **1**, 75–81 (1999).

70. O. D. Weiner, M. C. Rentel, A. Ott, G. E. Brown, M. Jedrychowski, M. B. Yaffe, S. P. Gygi, L. C. Cantley, H. R. Bourne, M. W. Kirschner, Hem-1 Complexes Are Essential for Rac Activation, Actin Polymerization, and Myosin Regulation during Neutrophil Chemotaxis. *PLoS Biol* **4**, e38 (2006).

71. A. Kawska, K. Carvalho, J. Manzi, R. Boujemaa-Paterski, L. Blanchoin, J.-L. Martiel, C. Sykes, How actin network dynamics control the onset of actin-based motility. *Proceedings of the National Academy of Sciences* **109**, 14440–14445 (2012).

72. K. B. Velle, L. K. Fritz-Laylin, Diversity and evolution of actin-dependent phenotypes. *Current Opinion in Genetics and Development* **58–59**, 40–48 (2019).

73. E. D. Goley, M. D. Welch, The ARP2/3 complex: An actin nucleator comes of age. *Nature Reviews Molecular Cell Biology* **7**, 713–726 (2006).

74. D. A. Valencia, M. E. Quinlan, Formins. *Current Biology* **31**, R517–R522 (2021).

75. D. R. Kovar, E. S. Harris, R. Mahaffy, H. N. Higgs, T. D. Pollard, Control of the Assembly of ATP- and ADP-Actin by Formins and Profilin. *Cell* **124**, 423–435 (2006).

76. J. Funk, F. Merino, L. Venkova, L. Heydenreich, J. Kierfeld, P. Vargas, S. Raunser, M. Piel, P. Bieling, Profilin and formin constitute a pacemaker system for robust actin filament growth. *eLife* **8**, e50963 (2019).

77. S. Dmitrieff, F. Nédélec, Amplification of actin polymerization forces. *Journal of Cell Biology* **212**, 763–766 (2016).

78. H. Nakamura, E. Rho, C. T. Lee, K. Itoh, D. Deng, S. Watanabe, S. Razavi, H. T. Matsubayashi, C. Zhu, E. Jung, P. Rangamani, S. Watanabe, T. Inoue, ActuAtor, a Listeria-inspired molecular tool for physical manipulation of intracellular organizations through de novo actin polymerization. *Cell Reports* **42**, 113089 (2023).

79. R. DeRose, T. Miyamoto, T. Inoue, Manipulating signaling at will: chemically-inducible dimerization (CID) techniques resolve problems in cell biology. *Pflugers Archiv : European journal of physiology* **465**, 409–417 (2013).

80. W. Luo, Z. Z. Lieu, E. Manser, A. D. Bershadsky, M. P. Sheetz, Formin DAAM1 organizes actin filaments in the cytoplasmic nodal actin network. *PLoS ONE* **11**, 1–22 (2016).

81. K. M. C. Chan, A. L. Arthur, J. Morstein, M. Jin, A. Bhat, D. Schlesinger, S. Son, D. A. Stevens, D. G. Drubin, D. A. Fletcher, Evolutionarily related small viral fusogens hijack distinct but modular actin nucleation pathways to drive cell-cell fusion. *Proc Natl Acad Sci USA* **118**, e2007526118 (2021).

82. A. Drazic, H. Aksnes, M. Marie, M. Boczkowska, S. Varland, E. Timmerman, H. Foyn, N. Glomnes, G. Rebowski, F. Impens, K. Gevaert, R. Dominguez, T. Arnesen, NAA80 is actin's N-terminal acetyltransferase and regulates cytoskeleton assembly and cell motility. *Proceedings of the National Academy of Sciences* **115**, 4399–4404 (2018).

83. J. Block, D. Breitsprecher, S. Kühn, M. Winterhoff, F. Kage, R. Geffers, P. Duwe, J. L. Rohn, B. Baum, C. Brakebusch, M. Geyer, T. E. B. Stradal, J. Faix, K. Rottner, FMNL2 Drives Actin-Based Protrusion and Migration Downstream of Cdc42. *Current Biology* **22**, 1005–1012 (2012).

84. A. Schirenbeck, R. Arasada, T. Bretschneider, M. Schleicher, J. Faix, Formins and VASPs may co-operate in the formation of filopodia. *Biochemical Society Transactions* **33**, 4 (2005).

85. H. Mizuno, C. Higashida, Y. Yuan, T. Ishizaki, S. Narumiya, N. Watanabe, Rotational movement of the formin mDia1 along the double helical strand of an actin filament. *Science* **331**, 80–83 (2011).

86. X. Naj, A. K. Hoffmann, M. Himmel, S. Linder, The formins FMNL1 and mDia1 regulate coiling phagocytosis of borrelia burgdorferi by primary human macrophages. *Infection and Immunity* **81**, 1683–1695 (2013).

87. C. J. Gould, S. Maiti, A. Michelot, B. R. Graziano, L. Blanchoin, B. L. Goode, The formin DAD domain plays dual roles in autoinhibition and actin nucleation. *Current Biology* **21**, 384–390 (2011).

88. M. P. Murrell, R. Voituriez, J.-F. Joanny, P. Nassoy, C. Sykes, M. L. Gardel, Liposome adhesion generates traction stress. *Nature Phys* **10**, 163–169 (2014).

89. A. Colin, T. Kotila, C. Guérin, M. Orhant-Prioux, B. Vianay, A. Mogilner, P. Lappalainen, M. Théry, L. Blanchoin, Recycling of the actin monomer pool limits the lifetime of network turnover. *The EMBO Journal* **42**, e112717 (2023).

90. D. Sakata, H. Taniguchi, S. Yasuda, A. Adachi-Morishima, Y. Hamazaki, R. Nakayama, T. Miki, N. Minato, S. Narumiya, Impaired T lymphocyte trafficking in mice deficient in an actin-nucleating protein, mDia1. *Journal of Experimental Medicine* **204**, 2031–2038 (2007).

91. C. Yang, L. Czech, S. Gerboth, S. Kojima, G. Scita, T. Svitkina, Novel Roles of Formin mDia2 in Lamellipodia and Filopodia Formation in Motile Cells. *PLoS Biol* **5**, e317 (2007).

92. Y. Shi, J. Zhang, M. Mullin, B. Dong, A. S. Alberts, K. A. Siminovitch, The mDial Formin Is Required for Neutrophil Polarization, Migration, and Activation of the LARG/RhoA/ROCK Signaling Axis during Chemotaxis. *The Journal of Immunology* **182**, 3837–3845 (2009).

93. T. Isogai, R. van der Kammen, D. Leyton-Puig, K. M. Kedziora, K. Jalink, M. Innocenti, Initiation of lamellipodia and ruffles involves cooperation between mDia1 and the Arp2/3 complex. *Journal of Cell Science*, jcs.176768 (2015).

94. P. Monzo, Y. K. Chong, C. Guetta-Terrier, A. Krishnasamy, S. R. Sathe, E. K. F. Yim, W. H. Ng, B. T. Ang, C. Tang, B. Ladoux, N. C. Gauthier, M. P. Sheetz, Mechanical confinement triggers glioma linear migration dependent on formin FHOD3. *MBoC* **27**, 1246–1261 (2016).

95. F. Kage, M. Winterhoff, V. Dimchev, J. Mueller, T. Thalheim, A. Freise, S. Brühmann, J. Kollasser, J. Block, G. Dimchev, M. Geyer, H.-J. Schnittler, C. Brakebusch, T. E. B. Stradal, M.-F. Carlier, M. Sixt, J. Käs, J. Faix, K. Rottner, FMNL formins boost lamellipodial force generation. *Nat Commun* **8**, 14832 (2017).

96. Y. Yamazaki, Y. Miyata, K. Morigaki, M. Miyazaki, Controlling Physical and Biochemical Parameters of Actin Nucleation Using a Patterned Model Lipid Membrane. *Nano Lett.* **24**, 1825–1834 (2024).

97. M. Abercrombie, J. E. M. Heaysman, S. M. Pegrum, The locomotion of fibroblasts in culture I. Movements of the leading edge. *Experimental Cell Research* **59**, 393–398 (1970).

98. P. Maiuri, E. Terriac, P. Paul-Gilloteaux, T. Vignaud, K. McNally, J. Onuffer, K. Thorn, P. A. Nguyen, N. Georgoulia, D. Soong, A. Jayo, N. Beil, J. Beneke, J. C. Hong Lim, C. Pei-Ying Sim, Y.-S. Chu, A. Jiménez-Dalmaroni, J.-F. Joanny, J.-P. Thiery, H. Erfle, M. Parsons, T. J. Mitchison, W. A. Lim, A.-M. Lennon-Duménil, M. Piel, M. Théry, The first World Cell Race. *Current Biology* **22**, R673–R675 (2012).

99. S. A. Koestler, K. Rottner, F. Lai, J. Block, M. Vinzenz, J. V. Small, F- and G-Actin Concentrations in Lamellipodia of Moving Cells. *PLoS ONE* **4**, e4810 (2009).

100. S. Samarin, S. Romero, C. Kocks, D. Didry, D. Pantaloni, M. F. Carlier, How VASP enhances actin-based motility. *Journal of Cell Biology* **163**, 131–142 (2003).

101. W. M. Brieher, M. Coughlin, T. J. Mitchison, Fascin-mediated propulsion of Listeria monocytogenes independent of frequent nucleation by the Arp2/3 complex. *Journal of Cell Biology* **165**, 233–242 (2004).

102. P. Li, S. Banjade, H. C. Cheng, S. Kim, B. Chen, L. Guo, M. Llaguno, J. V. Hollingsworth, D. S. King, S. F. Banani, P. S. Russo, Q. X. Jiang, B. T. Nixon, M. K. Rosen, Phase transitions in the assembly of multivalent signalling proteins. *Nature* **483**, 336–340 (2012).

103. C. Simon, R. Kusters, V. Caorsi, A. Allard, M. Abou-Ghali, J. Manzi, A. Di Cicco, D. Lévy, M. Lenz, J.-F. Joanny, C. Campillo, J. Plastino, P. Sens, C. Sykes, Actin dynamics drive cell-like membrane deformation. *Nature Physics* **15**, 602–609 (2019).

104. P. DiMilla, J. Stone, J. Quinn, S. Albelda, D. Lauffenburger, Maximal migration of human smooth muscle cells on fibronectin and type IV collagen occurs at an intermediate attachment strength. *Journal of Cell Biology* **122**, 729–737 (1993).

105. C. Schreiber, B. Amiri, J. C. J. Heyn, J. O. Rädler, M. Falcke, On the adhesion–velocity relation and length adaptation of motile cells on stepped fibronectin lanes. *Proc. Natl. Acad. Sci. U.S.A.* **118**, e2009959118 (2021).

106. V. Caorsi, J. Lemière, C. Campillo, M. Bussonnier, J. Manzi, T. Betz, J. Plastino, K. Carvalho, C. Sykes, Cell-sized liposome doublets reveal active tension build-up driven by acto-myosin dynamics. *Soft Matter* **12**, 6223–6231 (2016).

107. W. I. Goh, K. B. Lim, T. Sudhaharan, K. P. Sem, W. Bu, A. M. Chou, S. Ahmed, mDia1 and WAVE2 Proteins Interact Directly with IRSp53 in Filopodia and Are Involved in Filopodium Formation. *Journal of Biological Chemistry* **287**, 4702–4714 (2012).

108. A. Bisaria, A. Hayer, D. Garbett, D. Cohen, T. Meyer, Membrane-proximal F-actin restricts local membrane protrusions and directs cell migration. *Science* **368**, 1205–1210 (2020).

109. Z. Shi, Z. T. Graber, T. Baumgart, H. A. Stone, A. E. Cohen, Cell Membranes Resist Flow. *Cell* **175**, 1769-1779.e13 (2018).

110. S. Gat, C. Simon, C. Campillo, A. Bernheim-Groswasser, C. Sykes, Finger-like membrane protrusions are favored by heterogeneities in the actin network. *Soft Matter* **16**, 7222–7230 (2020).

111. S. M. Bartelt, J. Steinkühler, R. Dimova, S. V. Wegner, Light-Guided Motility of a Minimal Synthetic Cell. *Nano Lett.* **18**, 7268–7274 (2018).

112. L. A. Banaszynski, C. W. Liu, T. J. Wandless, Characterization of the FKBP·Rapamycin·FRB Ternary Complex. *J. Am. Chem. Soc.* **127**, 4715–4721 (2005).

113. E. Rihtar, T. Lebar, D. Lainšček, K. Kores, S. Lešnik, U. Bren, R. Jerala, Chemically inducible split protein regulators for mammalian cells. *Nat Chem Biol*, doi: 10.1038/s41589-022-01136-x (2022).

114. K. Yoshida, K. Abe, Y. Sato, I. Kawamata, R. J. Archer, H. T. Matsubayashi, S. Hamada, S. Murata, S. Nomura, Transmembrane DNA Sequence Signaling via Hybridization. ChemRxiv [Preprint] (2024). https://doi.org/10.26434/chemrxiv-2024-571kp.

115. S. L. Veatch, S. L. Keller, Separation of Liquid Phases in Giant Vesicles of Ternary Mixtures of Phospholipids and Cholesterol. *Biophysical Journal* **85**, 3074–3083 (2003).

116. T. Litschel, B. Ramm, R. Maas, M. Heymann, P. Schwille, Beating Vesicles: Encapsulated Protein Oscillations Cause Dynamic Membrane Deformations. *Angewandte Chemie International Edition* **57**, 16286–16290 (2018).

117. S. Takada, N. Yoshinaga, N. Doi, K. Fujiwara, Controlling the Periodicity of a Reaction–Diffusion Wave in Artificial Cells by a Two-Way Energy Supplier. *ACS Nano* **16**, 16853–16861 (2022).

118. S. D. Hansen, W. Y. C. Huang, Y. K. Lee, P. Bieling, S. M. Christensen, J. T. Groves, Stochastic geometry sensing and polarization in a lipid kinase–phosphatase competitive reaction. *Proceedings of the National Academy of Sciences of the United States of America* **116**, 15013–15022 (2019).

119. Y. Sato, M. Takinoue, Capsule-like DNA Hydrogels with Patterns Formed by Lateral Phase Separation of DNA Nanostructures. *JACS Au* **2**, 159–168 (2022).

120. B. Haller, K. Jahnke, M. Weiss, K. Göpfrich, I. Platzman, J. P. Spatz, Autonomous Directional Motion of Actin-Containing Cell-Sized Droplets. *Advanced Intelligent Systems* **3**, 2000190 (2021).

121. R. Sakamoto, Z. Izri, Y. Shimamoto, M. Miyazaki, Y. T. Maeda, Geometric trade-off between contractile force and viscous drag determines the actomyosin-based motility of a cell-sized droplet. *Proc. Natl. Acad. Sci. U.S.A.* **119**, e2121147119 (2022).

122. S. Brühmann, D. S. Ushakov, M. Winterhoff, R. B. Dickinson, U. Curth, J. Faix, Distinct VASP tetramers synergize in the processive elongation of individual actin filaments from clustered arrays. *Proc Natl Acad Sci USA* **114**, E5815–E5824 (2017).

123. J. E. Tropea, S. Cherry, D. S. Waugh, "Expression and Purification of Soluble His6-Tagged TEV Protease" in *High Throughput Protein Expression and Purification: Methods and Protocols*, S. A. Doyle, Ed. (Humana Press, Totowa, NJ, 2009; https://doi.org/10.1007/978-1-59745-196-3_19)*Methods in Molecular Biology*, pp. 297–307.

124. T. Inoue, W. D. Heo, J. S. Grimley, T. J. Wandless, T. Meyer, An inducible translocation strategy to rapidly activate and inhibit small GTPase signaling pathways. *Nature Methods* **2**, 415–418 (2005).

125. H. Onuma, T. Komatsu, M. Arita, K. Hanaoka, T. Ueno, T. Terai, T. Nagano, T. Inoue, Rapidly rendering cells phagocytic through a cell surface display technique and concurrent Rac activation. *Science Signaling* **7**, 1–8 (2014).

126. Cytoplasmic Actin: Purification and Single Molecule Assembly Assays | SpringerLink. https://link.springer.com/protocol/10.1007/978-1-62703-538-5_9.

127. L. K. Doolittle, M. K. Rosen, S. B. Padrick, Measurement and analysis of in vitro actin polymerization. *Methods in Molecular Biology*, doi: 10.1007/978-1-62703-538-5_16 (2013).

128. S. Razavi, T. Inoue, T. LUO, D. Robinson, Methods for making giant vesicles and their use (2024). https://patents.google.com/patent/US11951210B2/en.

129. J. Schindelin, I. Arganda-Carreras, E. Frise, V. Kaynig, M. Longair, T. Pietzsch, S. Preibisch, C. Rueden, S. Saalfeld, B. Schmid, J.-Y. Tinevez, D. J. White, V. Hartenstein, K. Eliceiri, P. Tomancak, A. Cardona, Fiji: an open-source platform for biological-image analysis. *Nature methods* **9**, 676–682 (2012).

130. H. T. Matsubayashi, J. Mountain, N. Takahashi, A. Deb Roy, T. Yao, A. F. Peterson, C. Saez Gonzalez, I. Kawamata, T. Inoue, Non-catalytic role of phosphoinositide 3-kinase in mesenchymal cell migration through non-canonical induction of p85β/AP2-mediated endocytosis. *Nat Commun* **15**, 2612 (2024).

131. L. A. Gross, G. S. Baird, R. C. Hoffman, K. K. Baldridge, R. Y. Tsien, The structure of the chromophore within DsRed, a red fluorescent protein from coral. *Proc Natl Acad Sci U S A* **97**, 11990–11995 (2000).

132. V. I. Martynov, A. P. Savitsky, N. Y. Martynova, P. A. Savitsky, K. A. Lukyanov, S. A. Lukyanov, Alternative Cyclization in GFP-like Proteins Family. *Journal of Biological Chemistry* **276**, 21012–21016 (2001).

Figure 1

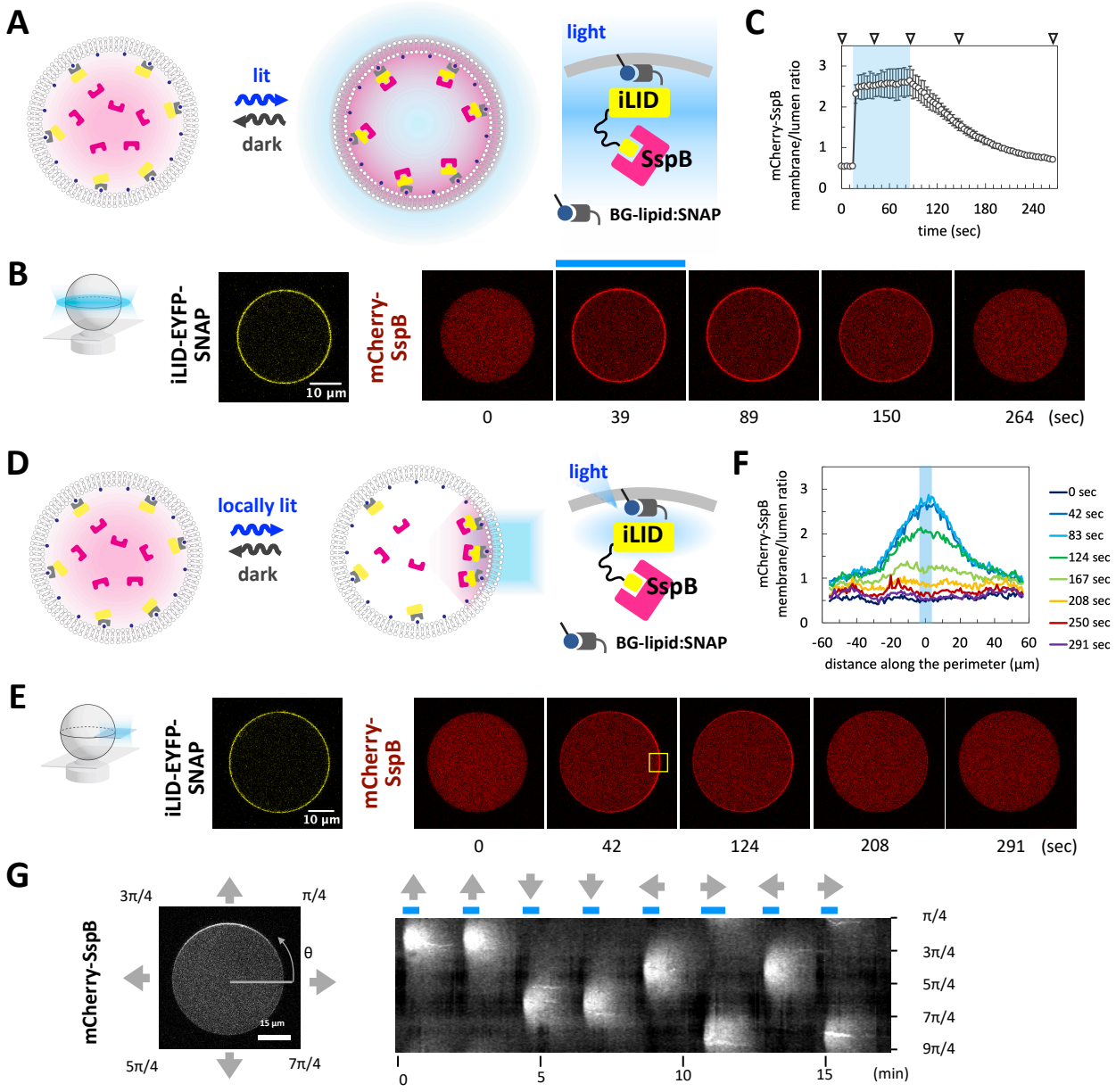

Fig. 1. Reversible and asymmetric control of protein localization with iLID-SspB within GUVs. (A) Schematic representation of iLID-SspB reaction with global light stimulation. iLID was tethered on the membrane via the interaction between SNAP-tag and bendylguanine-conjugated lipids. Upon blue light illumination, Jα helix of iLID extends to expose the binding site for SspB, whereas in the dark, iLID reverses to its closed state and releases SspB. (B) Representative images of iLID-YFP-SNAP and mCherry-SspB. Scale bar, 10 μm. Blue bar indicates the period of blue light illumination. (C) Time course of membrane/lumen ratio of mCherry-SspB signal (n=5). Error bars indicate standard deviation. Blue area indicates the period of blue light stimulation. Triangles indicate timepoints represented in (B). (D) Schematic representation of iLID-SspB reaction with local light stimulation. (E) Representative images of mCherry-SspB. Scale bar, 10 μm. Yellow box indicates the area of blue light illumination. (F) Membrane/lumen ratio of mCherry-SspB for the representative image shown. The distance is measured from the center of blue light illumination along the perimeter of the GUV. (G) Representative image and kymograph of repetitive and reversible SspB translocation. Kymograph shows membrane signal of mCherry-SspB.

Figure 2

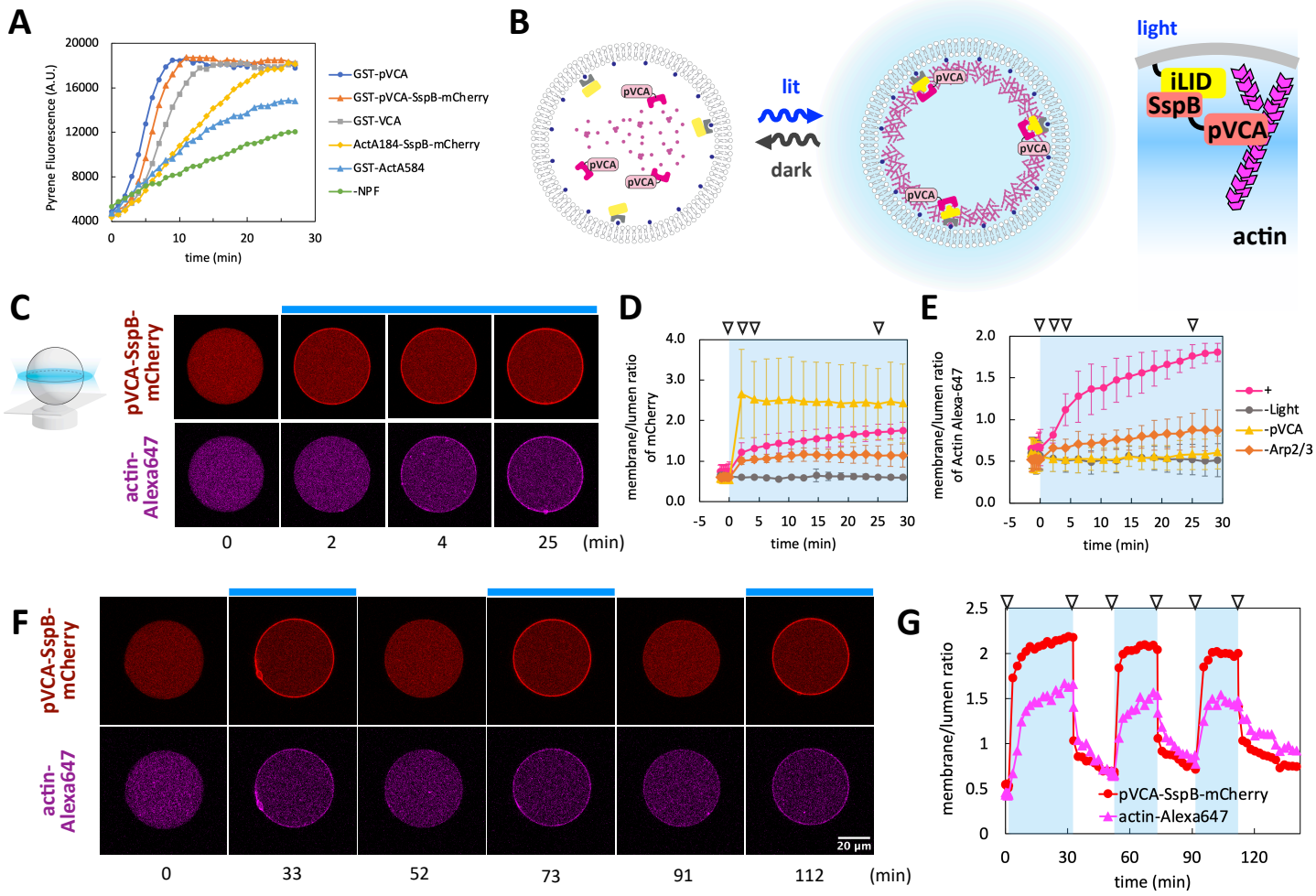

Fig. 2. Reversible light control of actin cytoskeleton within GUVs. (A) Bulk pyrene actin polymerization assay with 1 μM actin (5% pyrene labeled), 10 nM Arp2/3, and 100 nM NPFs. (-NPF) represents actin and Arp2/3 only condition. (B) Schematic representation of light inducible actin polymerization. Translocation of pVCA-SspB-mCherry increases local concentration of pVCA on the membrane and enhances actin polymerization. (C) Representative images of pVCA-SspB-mCherry and Alexa 647 actin. Blue bar indicates the period of blue light illumination. (D), (E) Time course of membrane/lumen ratio of mCherry and Alexa 647 actin. +: full set of components (n=4). -Light: no blue light stimulation (n=3). -pVCA: pVCA-SspB-mCherry was replaced with mCherry-SspB (n=4). -Arp2/3: Arp2/3 was omitted (n=4). Error bars indicate 95% CI. Triangles indicate timepoints represented in (C). (F) Representative images of reversible actin polymerization. Blue bars indicate the period of blue light illumination. (G) Time course of membrane/lumen ratio of pVCA-SspB-mCherry and Alexa 647-labeled actin in (F). Triangles indicate timepoints represented in (F).

Figure 3

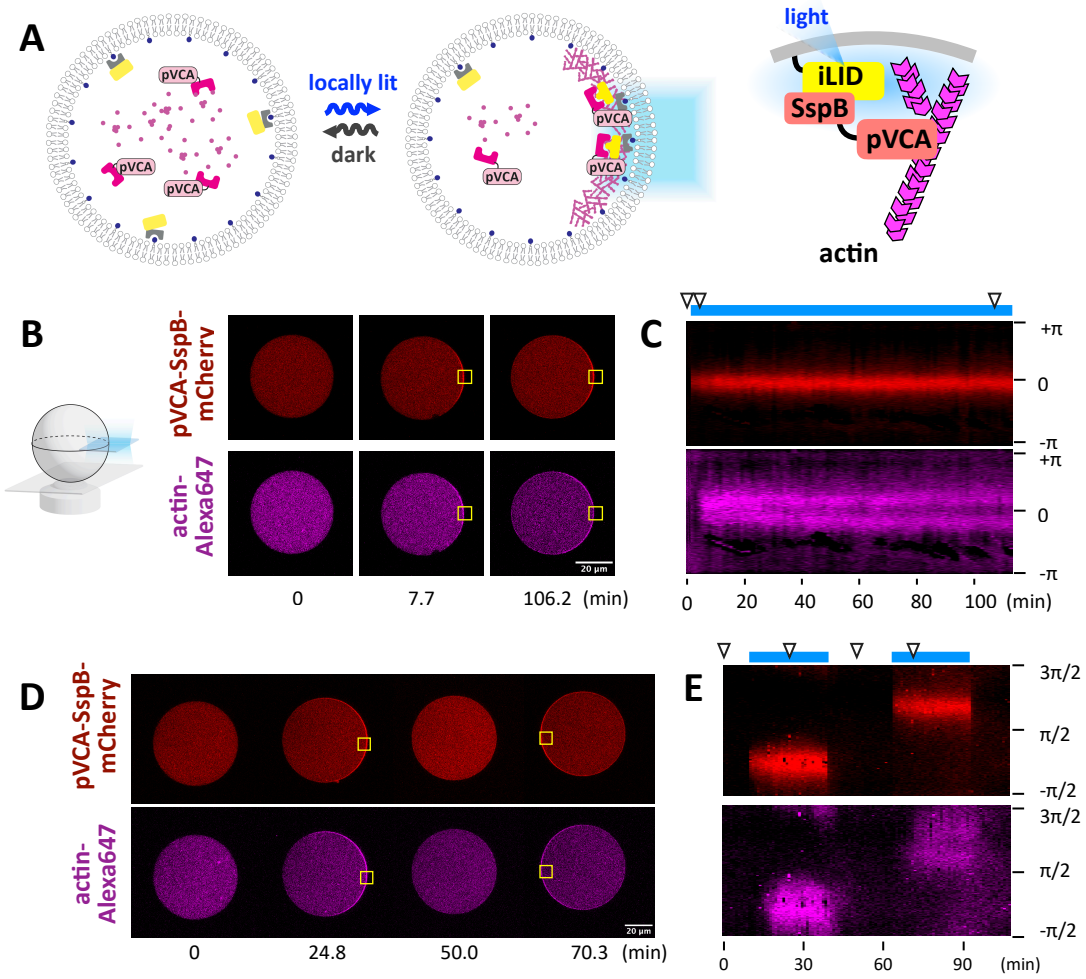

Fig. 3. Asymmetric light control of actin cytoskeleton within GUVs. (A) Schematic representation of iLID-SspB reaction with local light stimulation. (B, D) Representative images of light inducible asymmetric actin polymerization. Yellow boxes indicate the area of blue light illumination. (C, E) Kymograph of membrane pVCA-SspB and actin signals. Blue bars indicate the period of blue light illumination. Triangles indicate timepoints represented in (B, D).

Figure 4

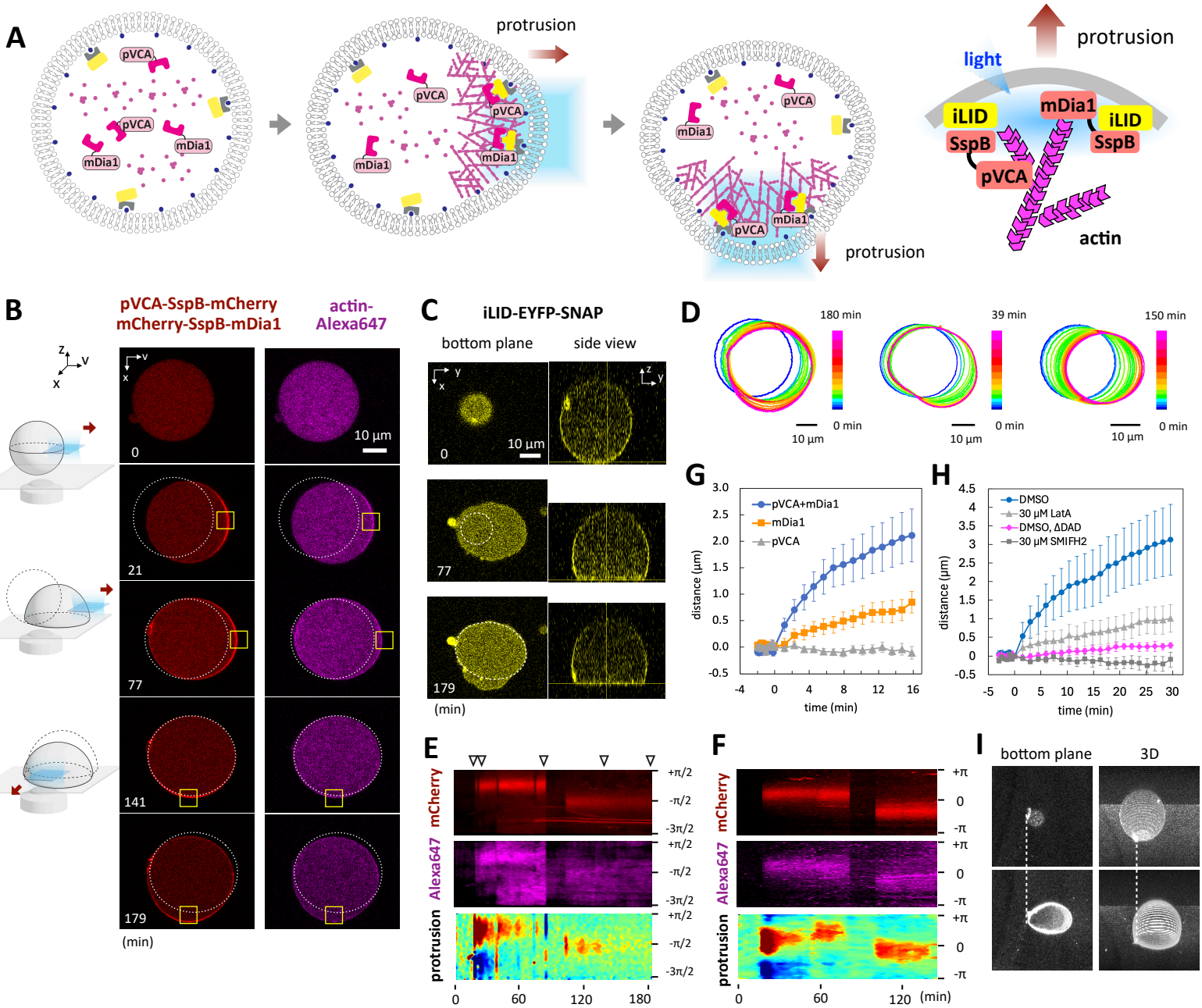

Fig. 4. mDia1-mediated actin polymerization drives protrusive motility of GUVs. (A) Schematic representation of light inducible membrane protrusion driven by pVCA and mDia1-mediated actin polymerization. (B) Representative images of pVCA-mDia1-mediated movement of GUVs. Yellow boxes indicate the area of blue light stimulation. Dotted line shows the initial position of the GUV. (C) Representative images of iLID-EYFP-SNAP showing the increase in adhesive area and vesicle deformation into dome-like shape. Bottom plane indicates the confocal plane right above the bottom substrate. Side view is reconstituted from z-stack. Dotted line shows the adhesive area of the previous images. (D) Color-coded boundaries of GUVs. The data correspond as follows. Left: Fig. 4B. Middle: Fig. S16A. Right: Fig. S16B. (E, F) Kymographs of membrane signal of mCherry and actin Alexa-647 and membrane protrusions. Triangles in (E) indicate the timepoints represented in (B, C). Data of (E) and (F) corresponds to Fig. 4 (B) and Fig. S16A, respectively. (G) Distance the front (illuminated) side of GUV membrane moved forward. pVCA+mDia1 (1 μM GST-pVCA-SspB-mCherry + 1 μM mCherry-SspB-mDia1, n=14 vesicles), mDia1 (1 μM mCherry-SspB-mDia1, n=12 vesicles), pVCA (1 μM GST-pVCA-SspB-mCherry, n=12 vesicles). Error bars indicate standard error of the mean (SEM). (H) DMSO (n=9 vesicles), 30 μM LatA (Latrunculin A) (n=10 vesicles). DMSO, ΔDAD: mCherry-SspB-mDia1 (FH1-FH2-DAD) was replaced with mCherry-SspB-mDia1(FH1-FH2) (n=13 vesicles). 30 μM SMIFH2 (n=6 vesicles). Error bars indicate standard error of the mean (SEM). (I) A GUV deformed into dome-like shape after movement. Upper images: before light stimulation. Lower images: after light stimulation. The data corresponds to Fig. S16C.

Figure S1

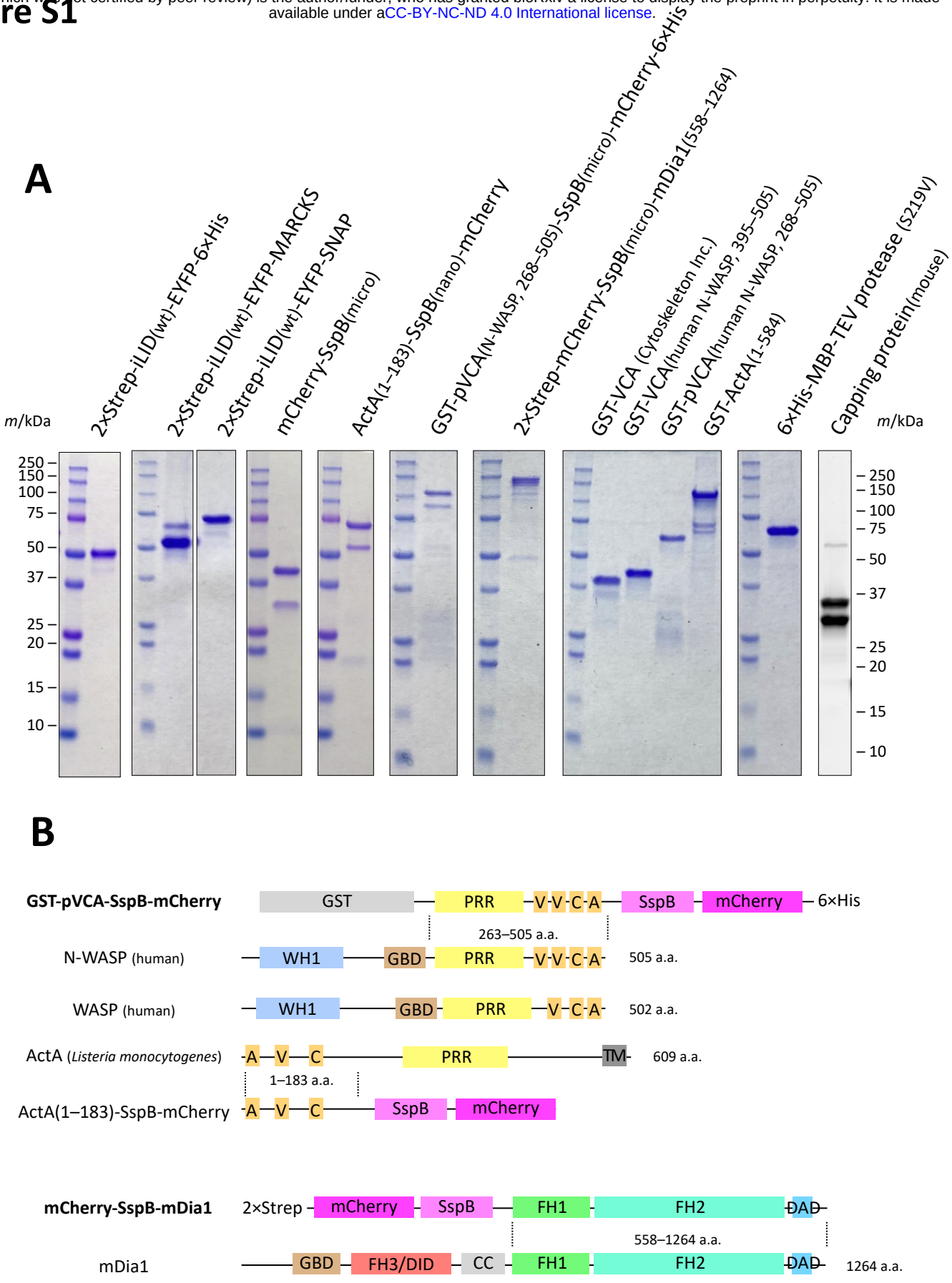

Fig. S1. Proteins purified in this study. (A) SDS-PAGE results of purified proteins. Blue: Coomassie brilliant blue staining. Gray: SYPRO Ruby staining. Most mCherry-tagged proteins show two extra bands due to a known chromophore cleavage reaction during the boiling process (131, 132). (B) Domain structures of NPFs used in this study.

Figure S2

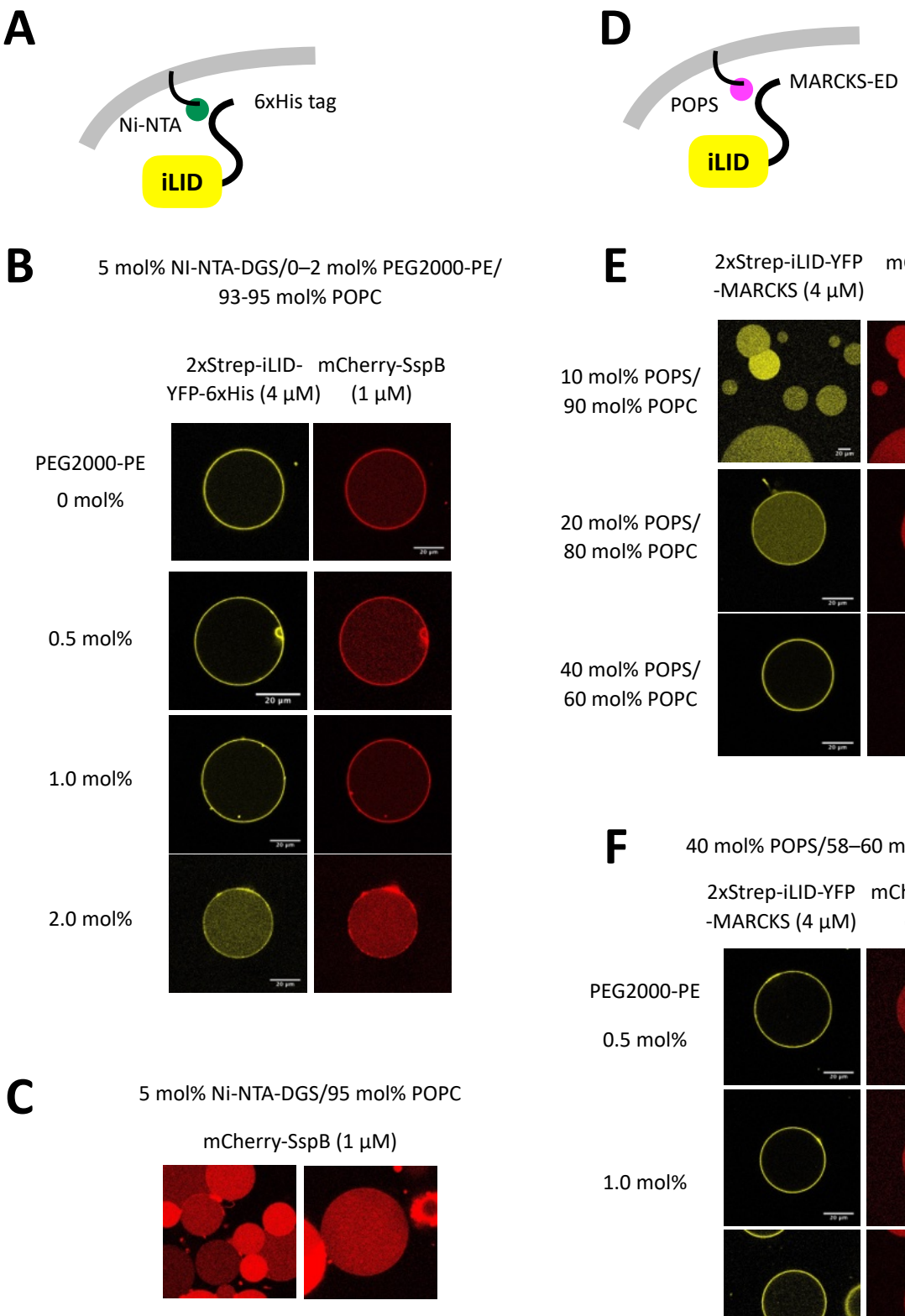

Figure S2

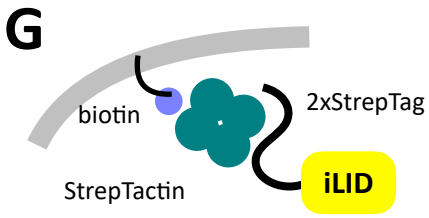

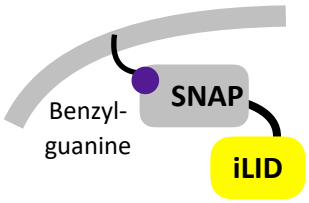

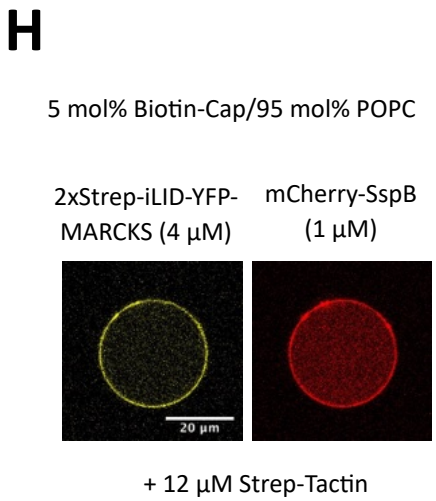

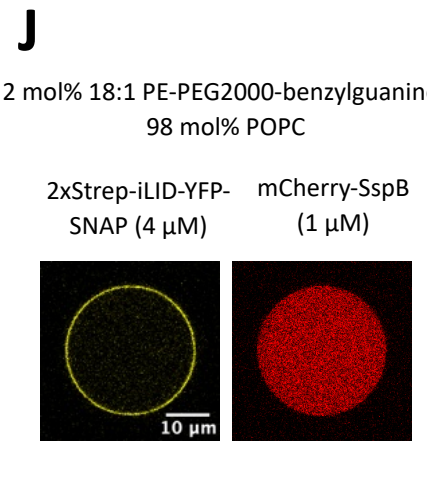

Fig. S2. Optimization of membrane anchoring of iLID. (A),(D),(G),(I): Schematic representations of membrane anchoring of iLID. (B),(C),(E),(F),(H),(J): Confocal images of iLID variants and mCherry-SspB. (B) His-tag Ni-NTA pair caused non-specific membrane recruitment of SspB. This is possibly caused by the presence of 2×Strep-iLID-YFP-6×His because mCherry-SspB itself did not show non-specific binding to the membrane of 5%Ni-NTA DGS/95%POPC (C). (E),(F) MARCKS-ED peptide requires high percentage of PS and PEGylated-lipids to reduce non-specific binding of SspB. (H) Biotin-StrepTactin-Streptag also caused non-specific membrane binding of SspB. (J) The data correspond with Fig. 1B.

Figure S3

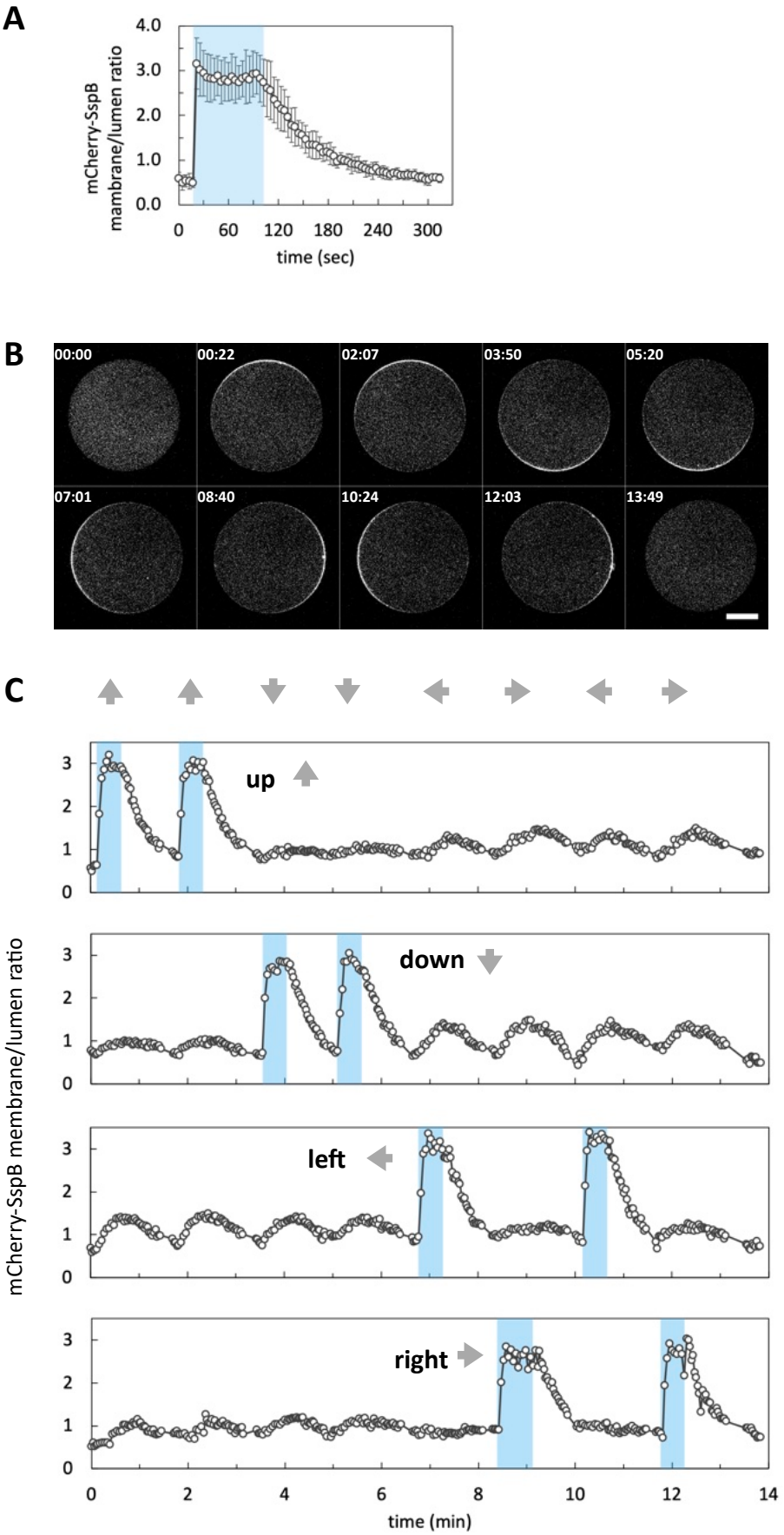

Fig. S3. Asymmetric control of protein localization with iLID-SspB within GUVs. (A) Time course of membrane/lumen ratio of mCherry-SspB signal in the illuminated area (n=5). Error bars indicate 95% CI. Blue area indicates the time window of blue light stimulation. The data corresponds to Fig. 1E and F. (B, C) Confocal images and time course of membrane/lumen ratio of mCherry-SspB signal responding to repetitive local light illuminations. The data corresponds to Fig. 1G.

Figure S4

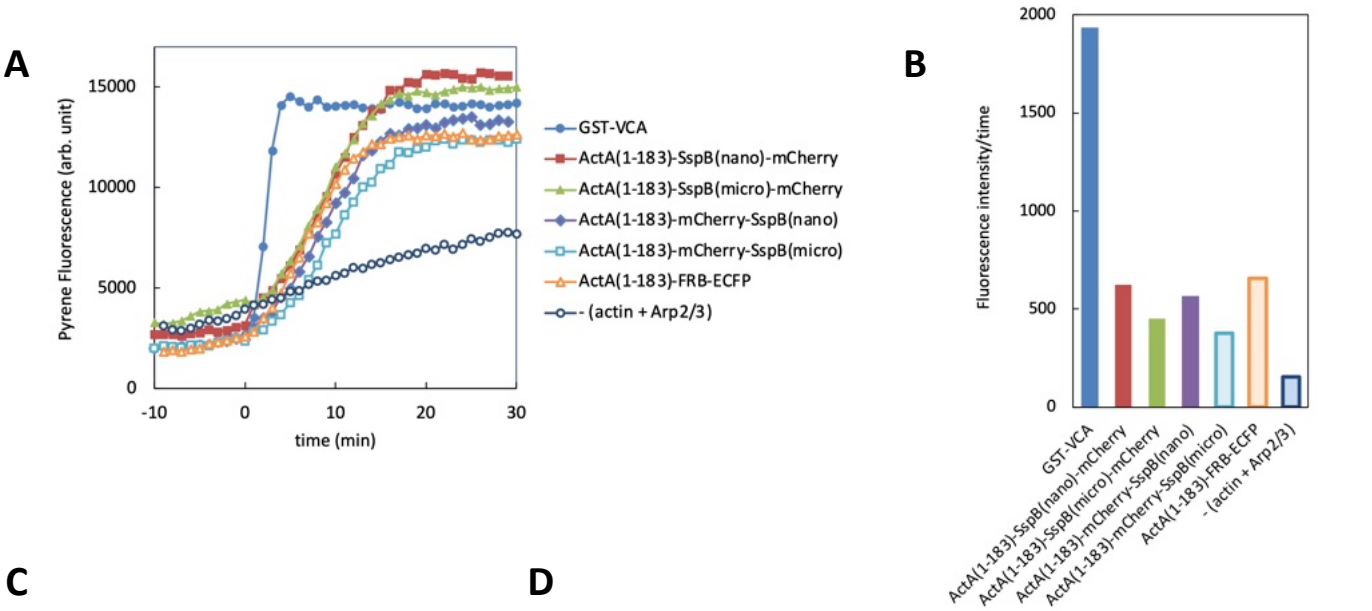

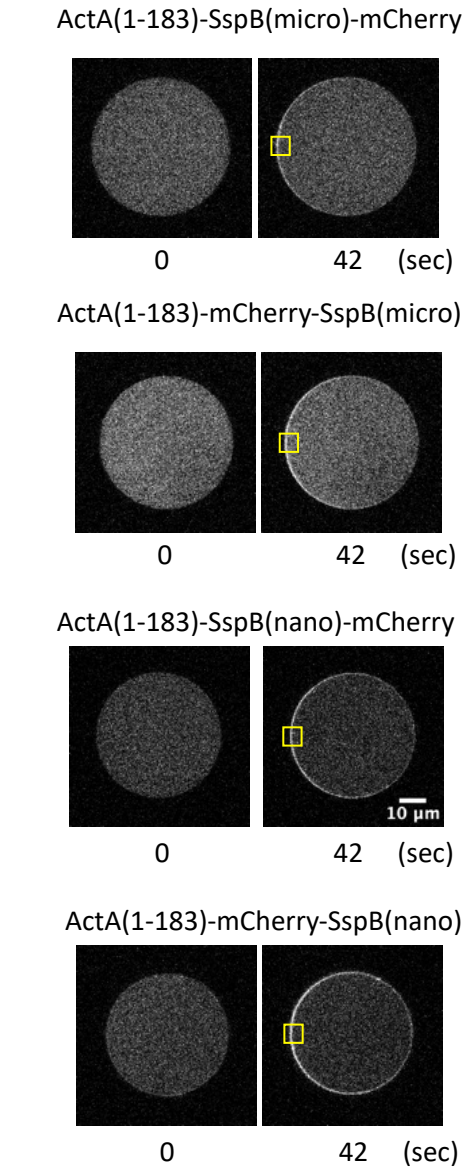

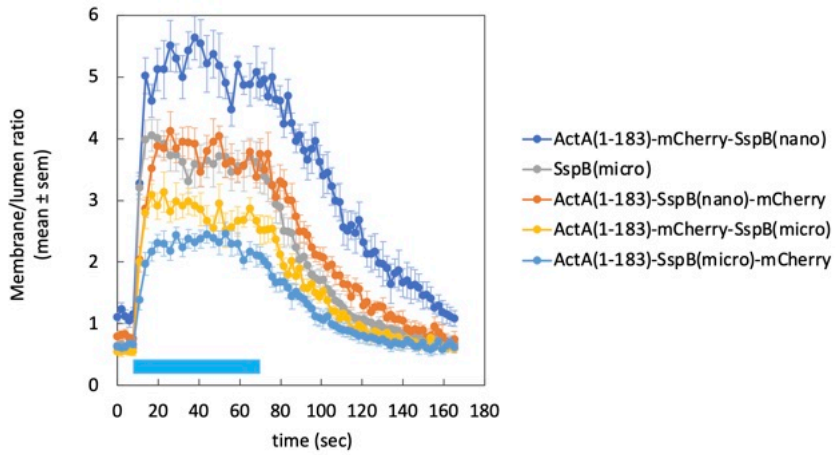

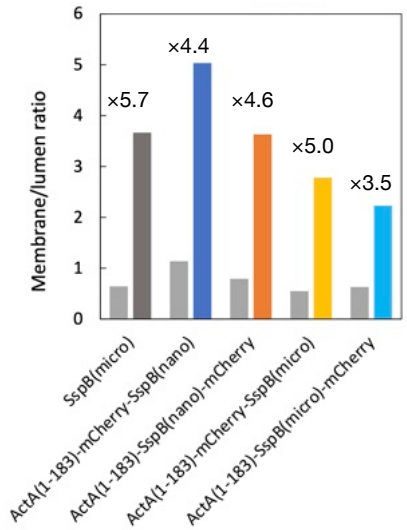

Fig. S4. Optimization of ActA-SspB. (A) Pyrene actin polymerization assay. The reaction was performed with 1 μM actin (5% pyrene labeled), 10 nM Arp2/3, and 100 nM ActA variants or GST-VCA. (B) Fluorescence intensity/time in 0–6 min of (A) was plotted as bar chart. (C–E) Light inducible local membrane recruitment of ActA (C) Confocal images of ActA translocation. Yellow boxes indicate the area of blue light illumination. (D) Time course of membrane/lumen ratio of ActA-SspB variants (n≥5 for each variant). Error bars indicate SEM. Blue bar indicates the time window of blue light stimulation. (E) Average membrane/lumen ratio of mCherry signal. In each condition, left and right bars indicate before and after light stimulation, respectively. The numbers on the bar chart indicate the fold change after stimulation.

Figure S5

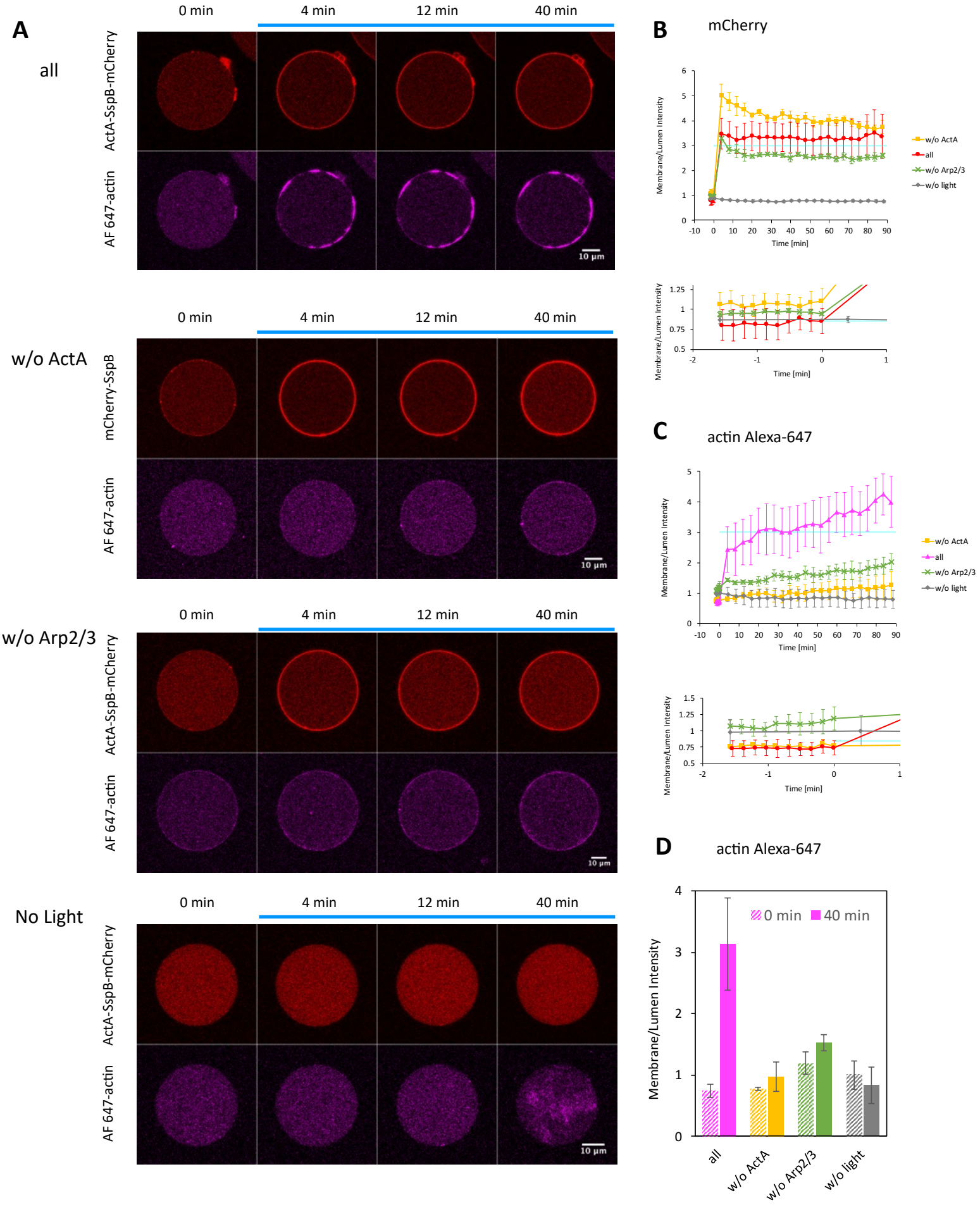

Figure S5

Fig S5. Light inducible actin polymerization with global ActA membrane recruitment. iLID-EYFP-MARCKS (5 µM), ActA-SspBnano-mCherry (2 µM), actin (1.5 µM, 10% Alexa-647 labeled), and Arp2/3 (150 nM) were encapsulated in GUVs containing 60 mol% POPC/40 mol% POPS. Blue light was applied to the entire GUV. (A) Representative images of ActA(1–183)-SspB(nano)-mCherry and actin Alexa-647. All components (n=4): w/o ActA: ActA(1–183)-SspB(nano)-mCherry was replaced with mCherry-SspB(micro) (n=3), w/o Arp2/3: Arp2/3 was omitted (n=3). No Light: no blue light stimulation (n=3). (B, C) Time course of membrane/lumen ratio of mCherry and actin Alexa 647. (D) Bar chart of membrane/lumen ratio of actin Alexa 647 before (0 min) and after (40 min) light stimulation. Error bars indicate SEM.

Figure S6

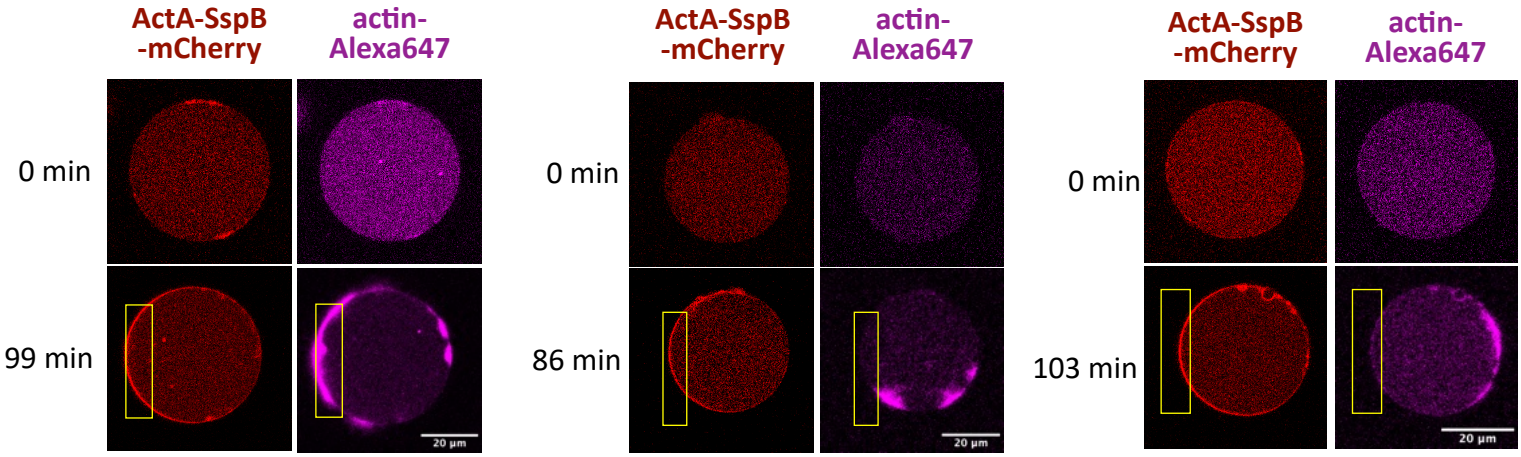

Fig S6. Asymmetric ActA membrane recruitment fails to induce directed actin polarization toward local light illumination. iLID-EYFP-MARCKS (5 μM), ActA-SspBnano-mCherry (2 μM), actin (1.5 μM, 10% Alexa-647 labeled), and Arp2/3 (150 nM), 1 mM ATP were encapsulated in GUVs containing 60 mol% POPC/40 mol% POPS. Yellow boxes indicate the area of blue light illumination. Although ActA creates asymmetric distribution, actin patches randomly distributed due to the diffusion on the membrane.

Figure S7

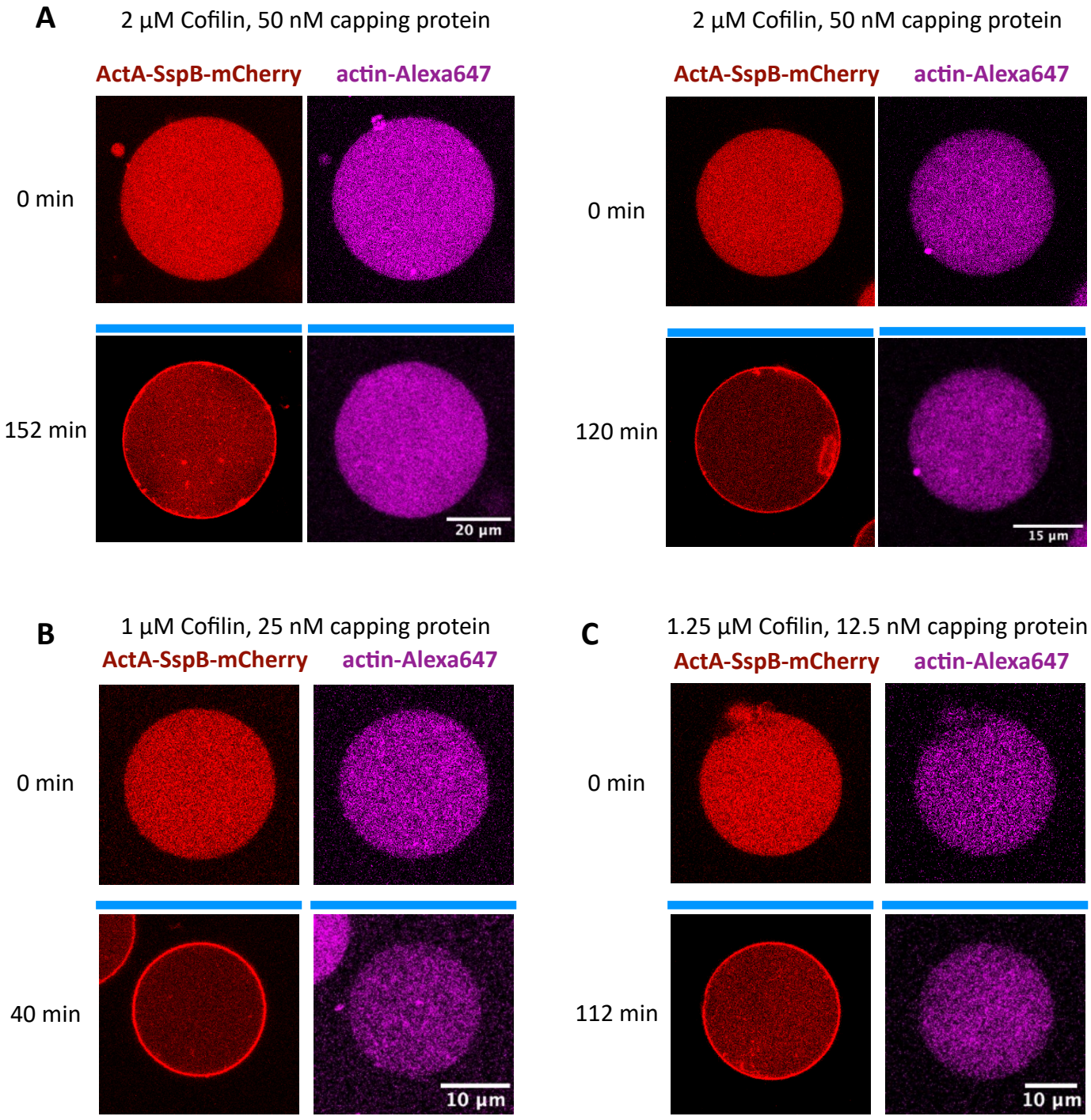

Fig. S7. Global ActA membrane recruitment fails to induce actin polymerization on the membrane in the presence of profilin, cofilin, and capping protein. 15 µM iLID-YFP-MARCKS, 5 µM ActA(1-183)-SspB(nano)-mCherry, 7.5 µM actin (10% Alexa 647 labeled), 150 nM Arp2/3, 3 µM profilin, cofilin, and capping protein were encapsulated in GUVs containing 60 mol% POPC/40 mol% POPS. Blue bars indicate the period of blue light illumination.

Figure S8

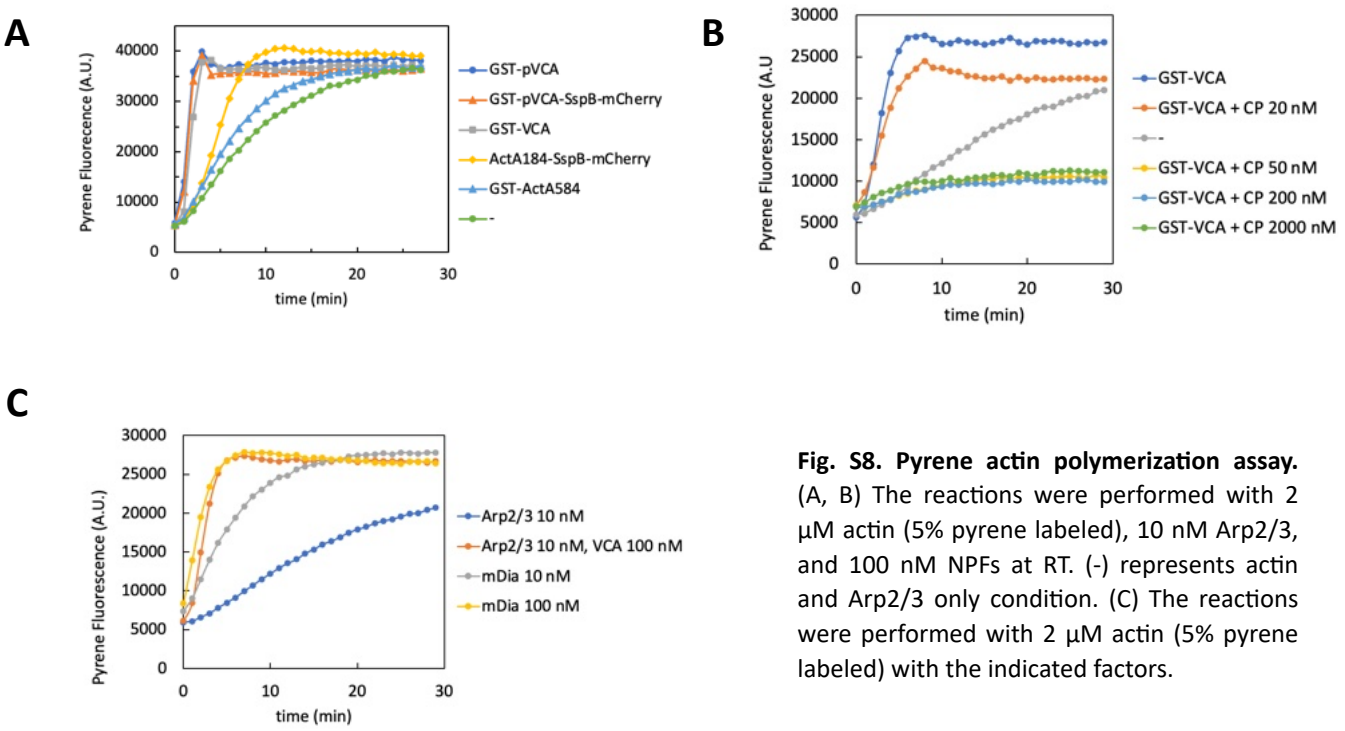

Fig. S8. Pyrene actin polymerization assay. (A, B) The reactions were performed with 2 µM actin (5% pyrene labeled), 10 nM Arp2/3, and 100 nM NPFs at RT. (-) represents actin and Arp2/3 only condition. (C) The reactions were performed with 2 µM actin (5% pyrene labeled) with the indicated factors.

Figure S9

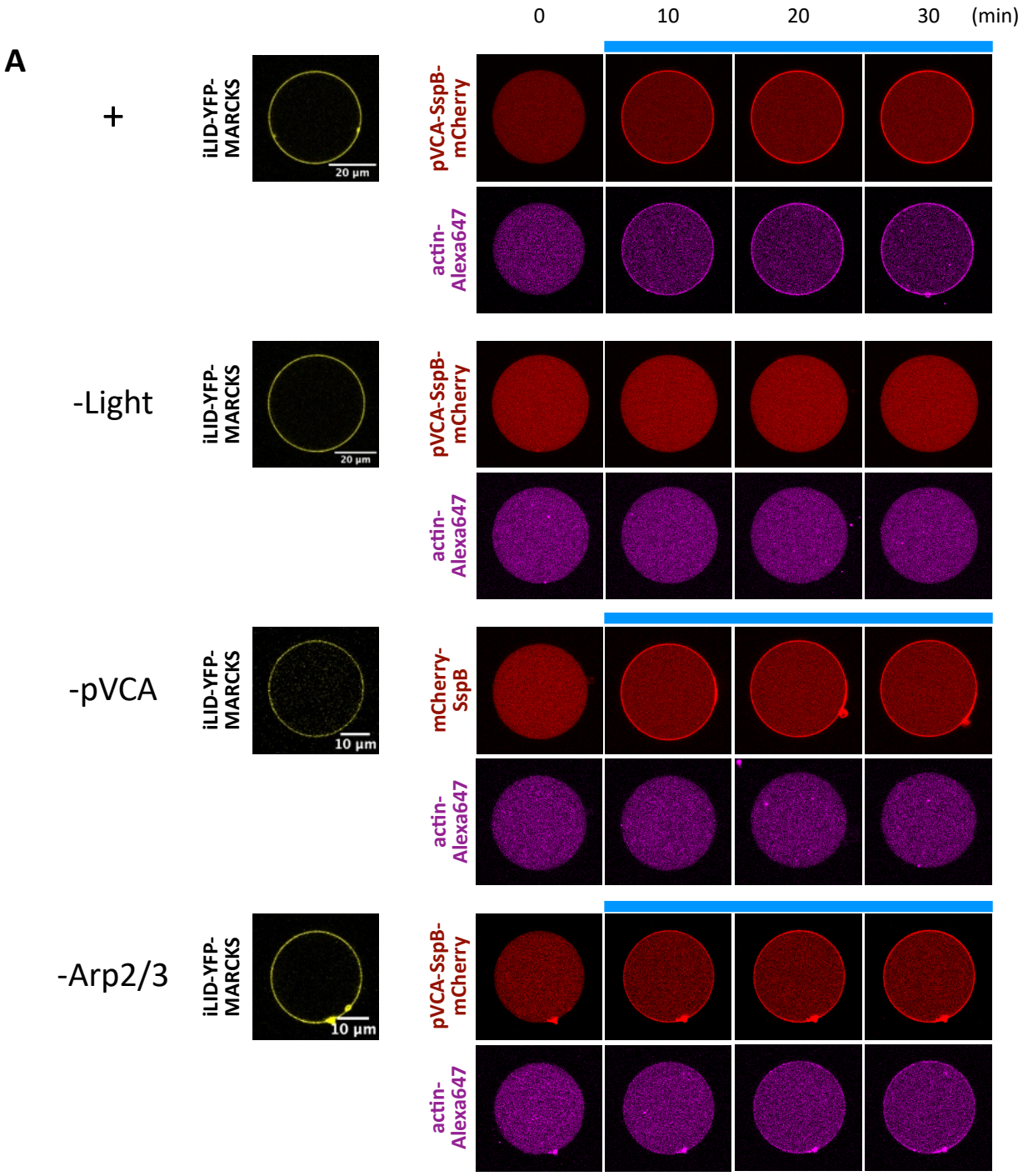

Fig. S9. Light control of actin cytoskeleton with pVCA-SspB-mCherry. The **d**ata correspond to Fig. 2C–E. (+) condition contains 15 µM iLID-YFP-MARCKS, 4.2 µM pVCA-SspB(nano)-mCherry, 7.5 µM actin (10% Alexa 647 labelled), 150 nM Arp2/3, 100 nM capping protein, 3 µM profilin, 4 µM cofilin, and 1 mM ATP. In (-light) and (-Arp2/3) conditions, blue light illumination or Arp2/3 was omitted from (+) condition, respectively. In (-pVCA) condition, pVCA-SspB(nano)-mCherry was replaced with mCherry-SspB(micro).

Figure S10

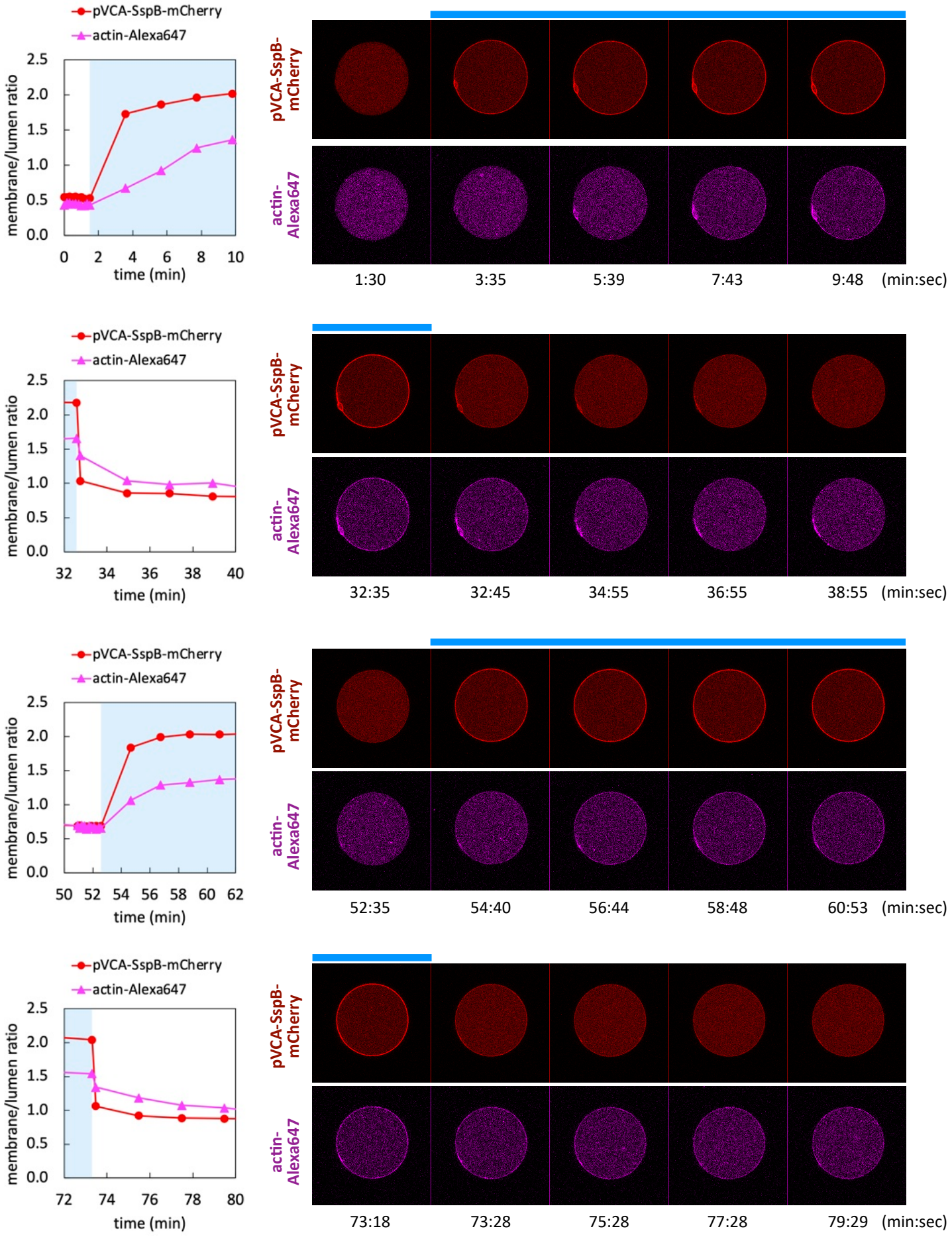

Figure S10

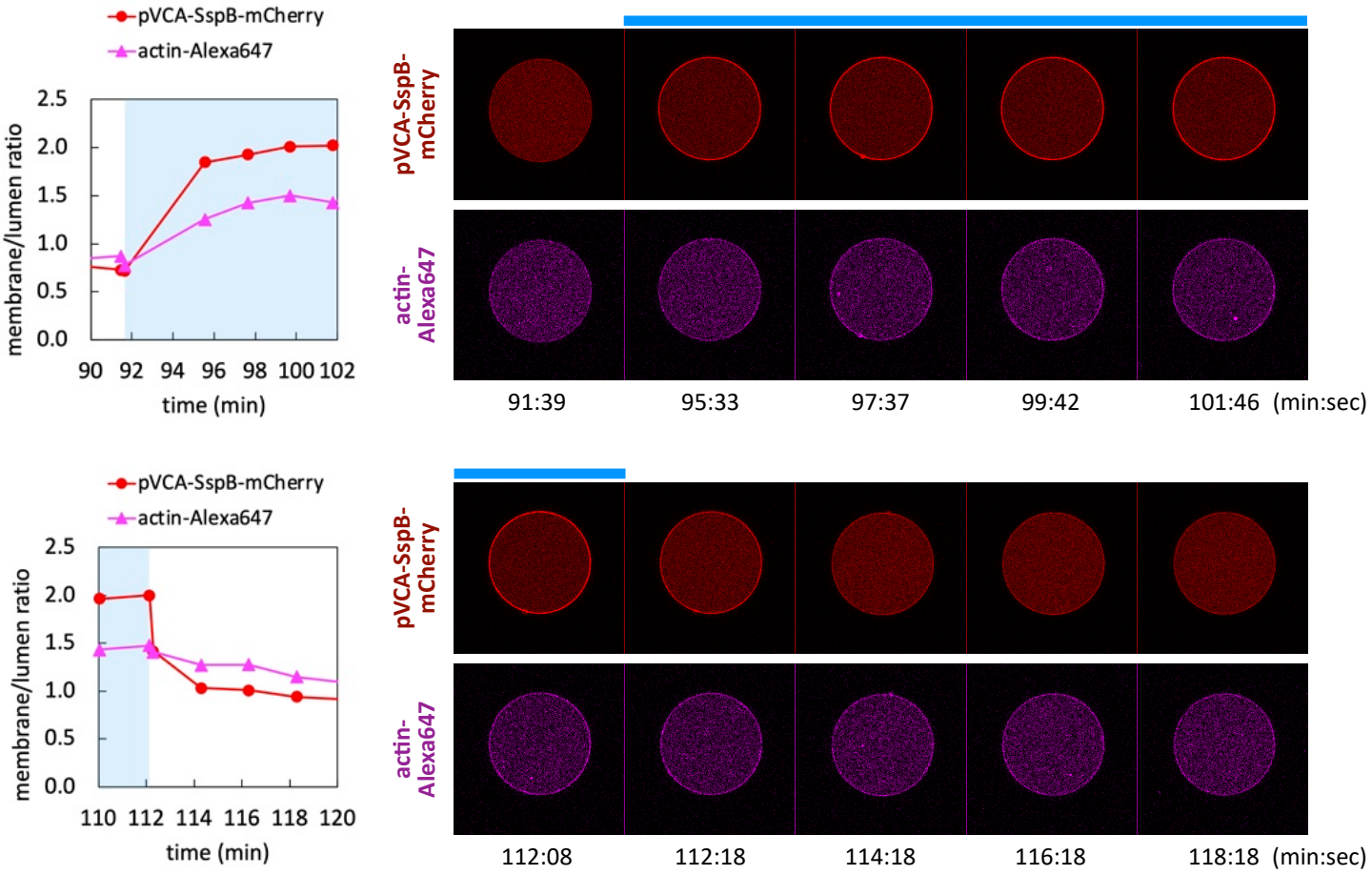

Fig. S10. Representative images of reversible actin polymerization. Confocal images and time course of membrane/lumen ratio of pVCA-SspB-mCherry and Alexa 647-labeld actin. Blue bars on images and blue regions in graphs indicate timepoints with blue light illumination. This figure corresponds with Fig. 2F, G.

Figure S11

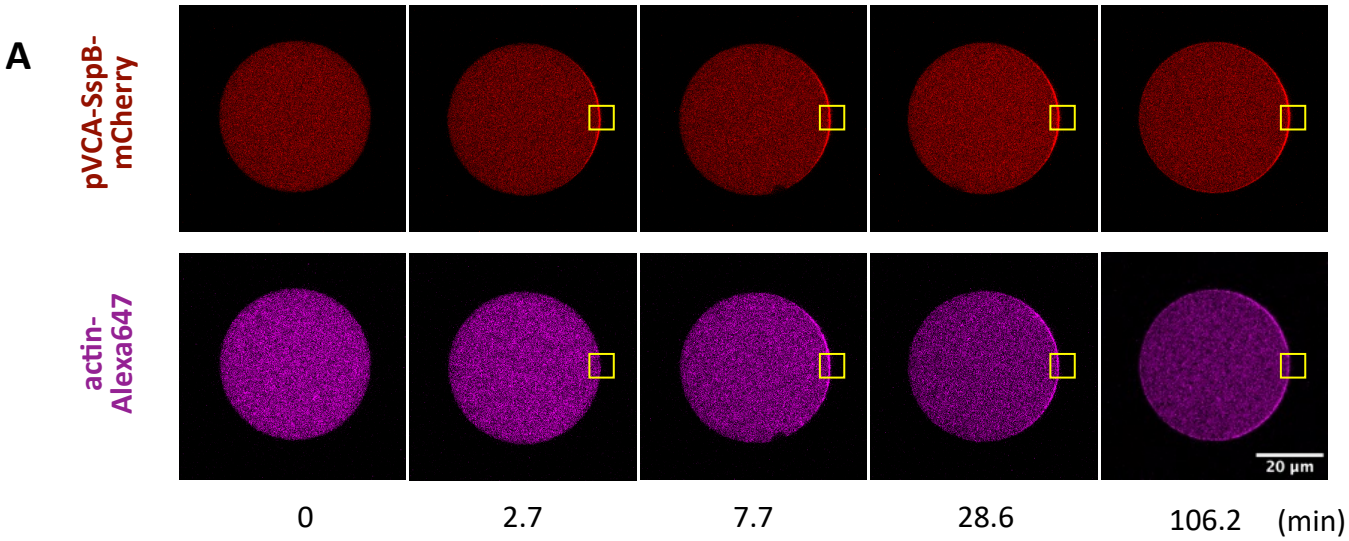

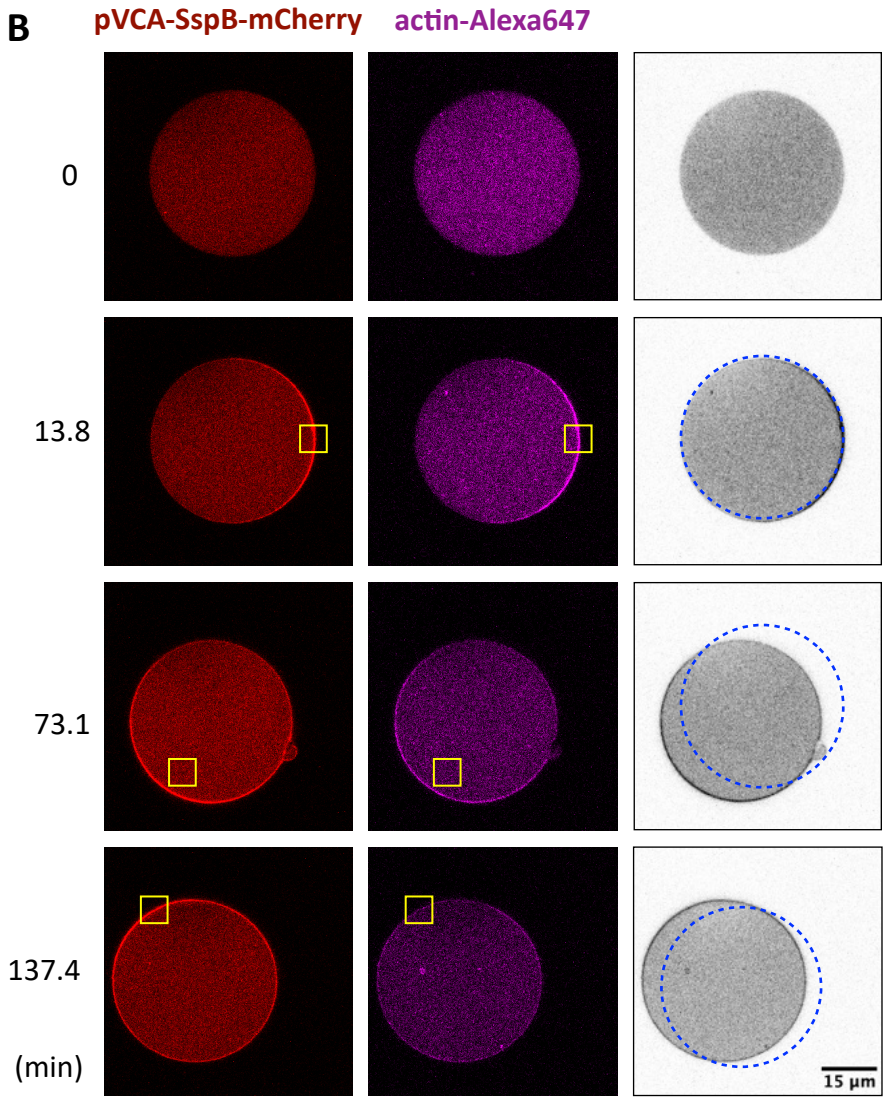

Fig. S11. Asymmetric actin polymerization induced by pVCA. (A, B) Confocal images of local pVCA recruitment and actin polymerization. Yellow boxes indicate areas of blue light illumination. (A) The data corresponds to Fig. 3B and C. In (B), Vesicle movement toward light stimulation was observed. Gray scaled images were created by averaging pVCA and actin images. Dotted circles indicate positions of vesicles in the images of one above.

Figure S12

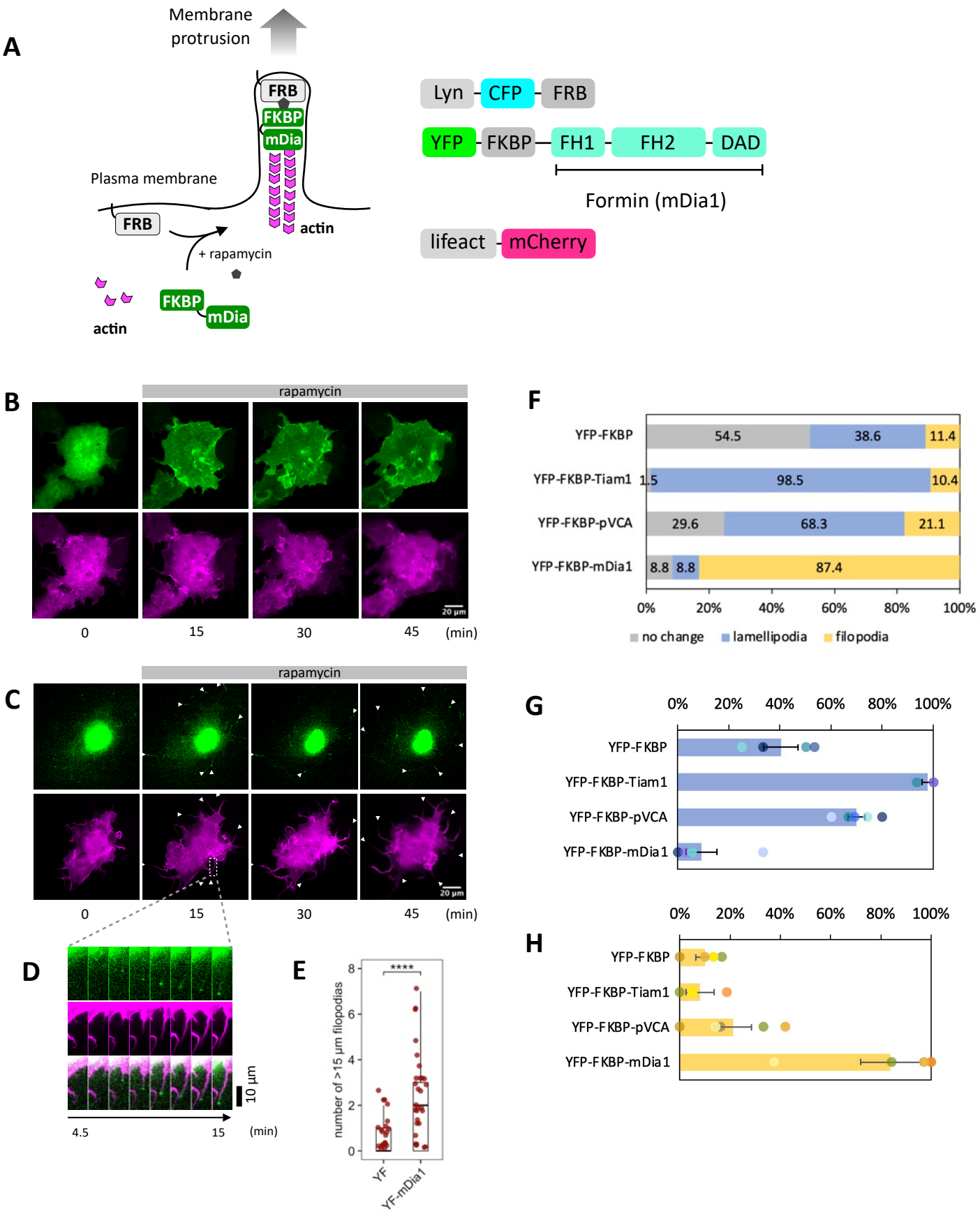

Figure S12

Fig. S12. Quantitative analysis of mDia1-induced filopodia formation in Cos7 cells. (A) Schematic representation of chemically-inducible mDia1 translocation and membrane protrusions. (B, C) Confocal images of plasma membrane recruitment of mDia1 and subsequent filopodia formation. Cos7 cells were transfected with Lyn-ECFP-FRB, Lifeact-mCherry, and either of YFP-FKBP or YFP-FKBP-mDia1. At time 0, 100 nM rapamycin was added. Green: YFP-FKBP or YFP-FKBP-mDia1. Magenta: Lifeact-mCherry. (B) YFP-FKBP control. (C) YFP-FKBP-mDia1. (D) Zoomed-up view of filopodia extension. Images were acquired every 1.5 minutes. The bottom is merged image. (E) Quantification of mDia1-induced filopodia. Number of filopodia whose length is longer than 15 µm was counted. P-values: ****: < 0.0001. Wilcoxon rank sum test. YF (YFP-FKBP): n=36 cells. YF-mDia1 (YFP-FKBP-mDia1): n=33 cells. (F–H) Quantification of the phenotypes observed after plasma membrane translocation of mDia1, pVCA, Tiam1 (Rac1 GEF), and control protein YFP-FKBP.

Figure S13

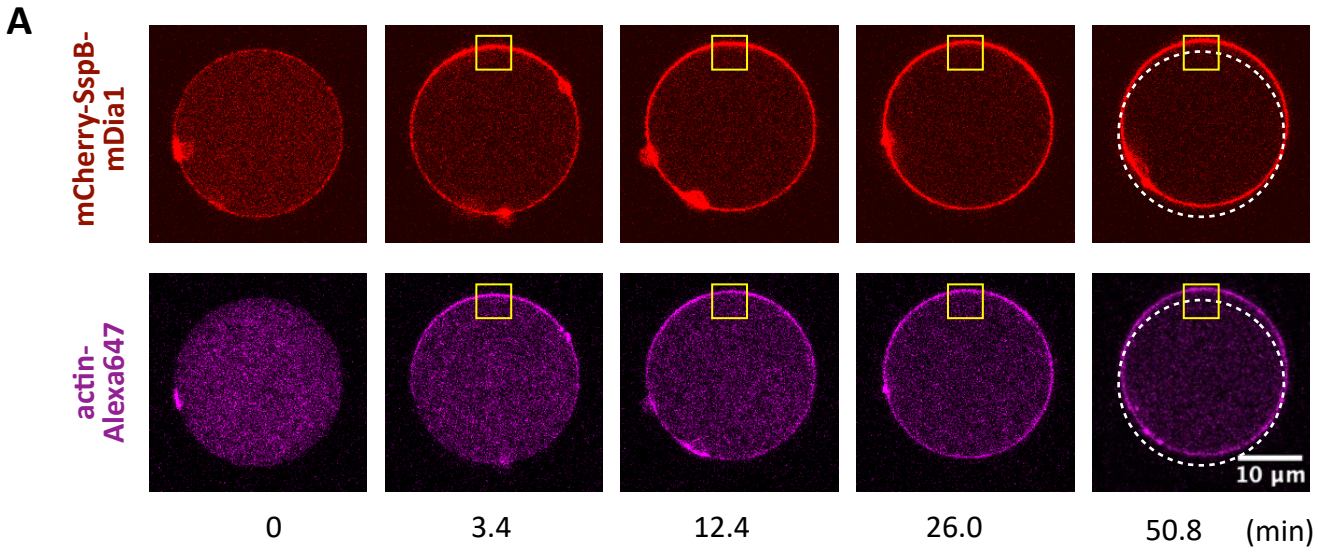

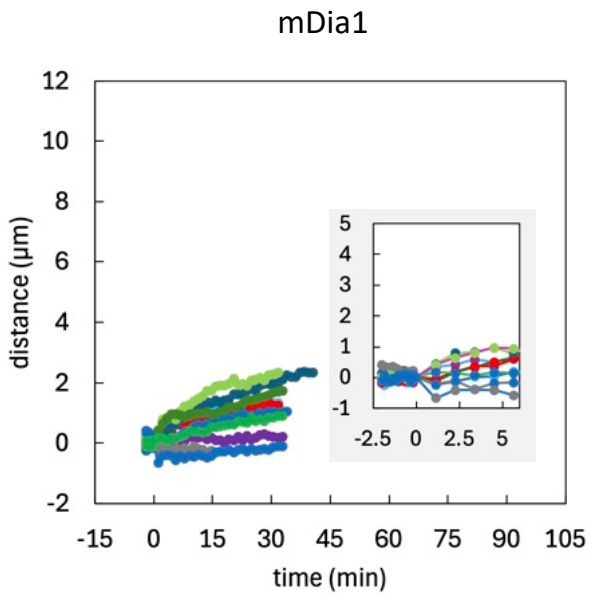

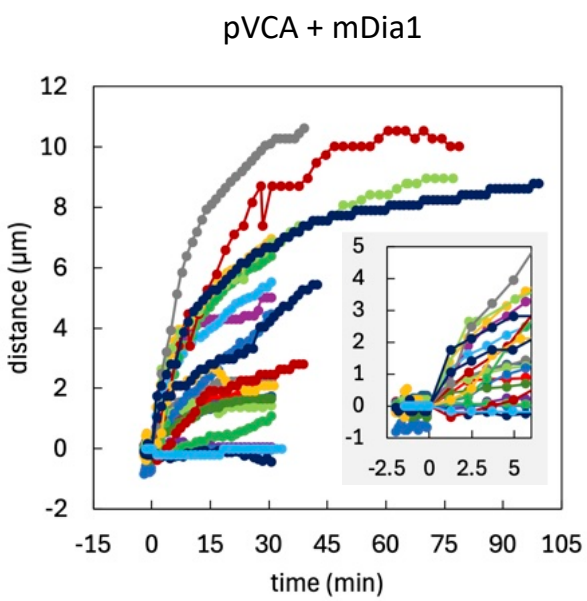

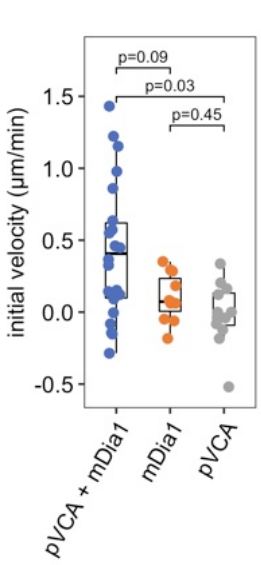

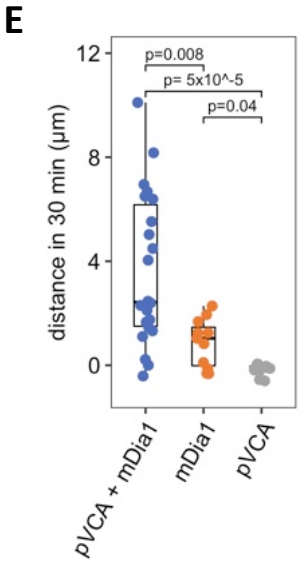

Fig. S13. mDia1-mediated GUV movement and the comparison between mDia1 and pVCA + mDia1 system. (A) Representative images of mDia1-mediated GUV movement. Yellow boxes indicate the area of blue light stimulation. Dotted lines indicate the initial position of the GUV. (B, C) Time course of the distance the front (illuminated) side of GUV membrane moved forward. Each line represents each GUVs. Insets show the initial response. (D, E) Quantification of the initial velocity and the distance the front side of GUV membrane moved forward. P values of Steel-Dwass test (two sided) are indicated. pVCA + mDia1: n=22 vesicles. mDia1: n=11 vesicles. pVCA: n=12 vesicles. Box whisker plots represent median, 1st, 3rd quartiles and 1.5×inter-quartile range.

Figure S14

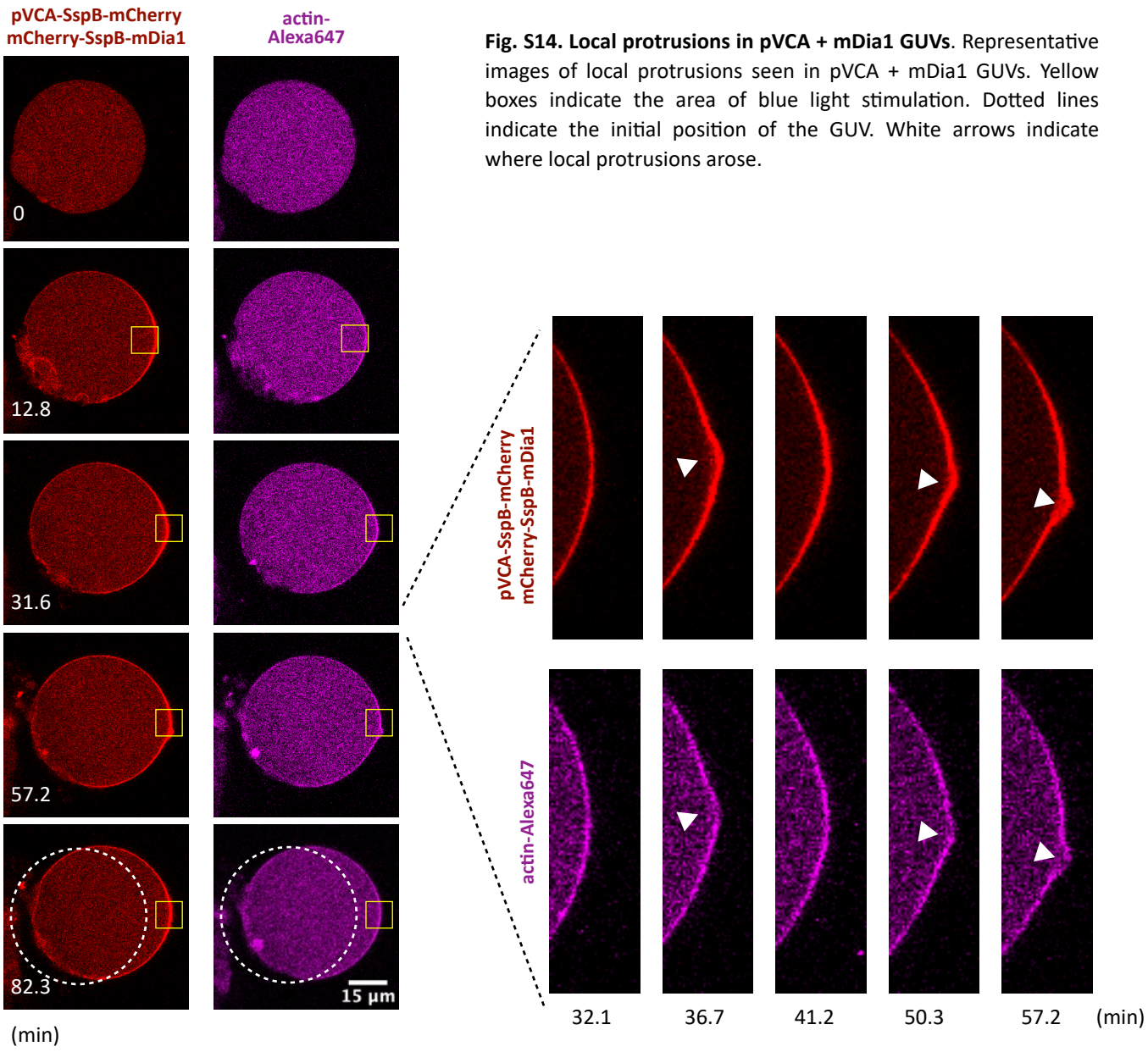

Fig. S14. Local protrusions in pVCA + mDia1 GUVs. Representative images of local protrusions seen in pVCA + mDia1 GUVs. Yellow boxes indicate the area of blue light stimulation. Dotted lines indicate the initial position of the GUV. White arrows indicate where local protrusions arose.

Figure S15

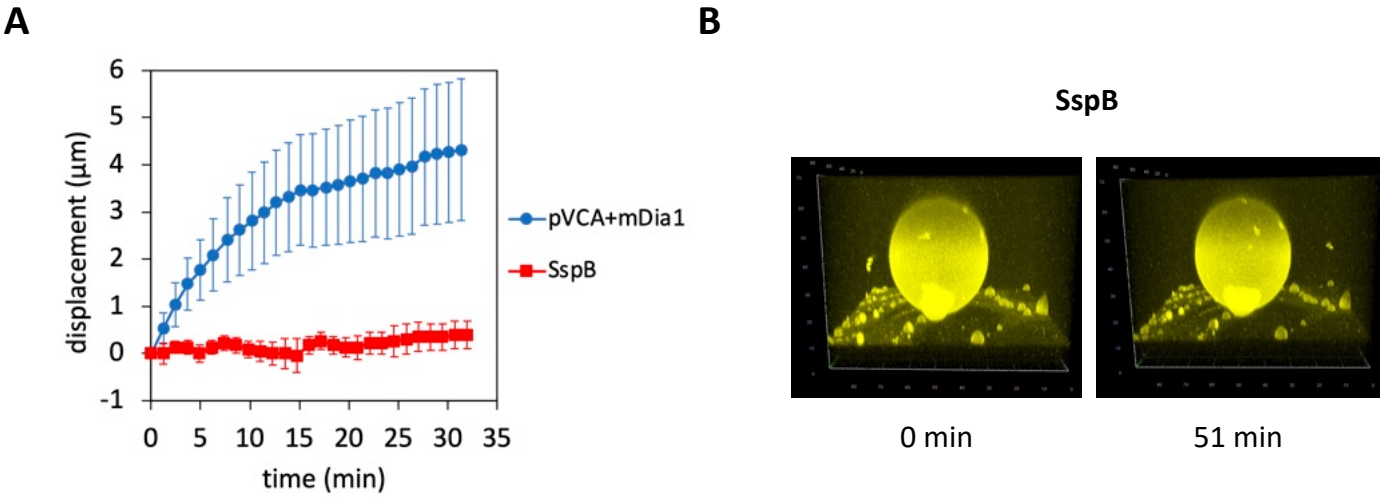

Fig. S15. Lack of vesicle movement and shape change with mCherry-SspB. With pVCA-SspB-mCherry and mCherry-SspB-mDia1 being replaced with mCherry-SspB, GUVs neither moved nor changed their shape after blue light illumination. (A) Time course of the distance the front (illuminated) side of GUV membrane moved forward. pVCA + mDia1 GUVs: n=6 vesicle. SspB GUVs: n=4 vesicles. Error bars indicate SEM. (B) 3D reconstitution of iLID-YFP-SNAP images before and after blue light illumination.

Figure S16

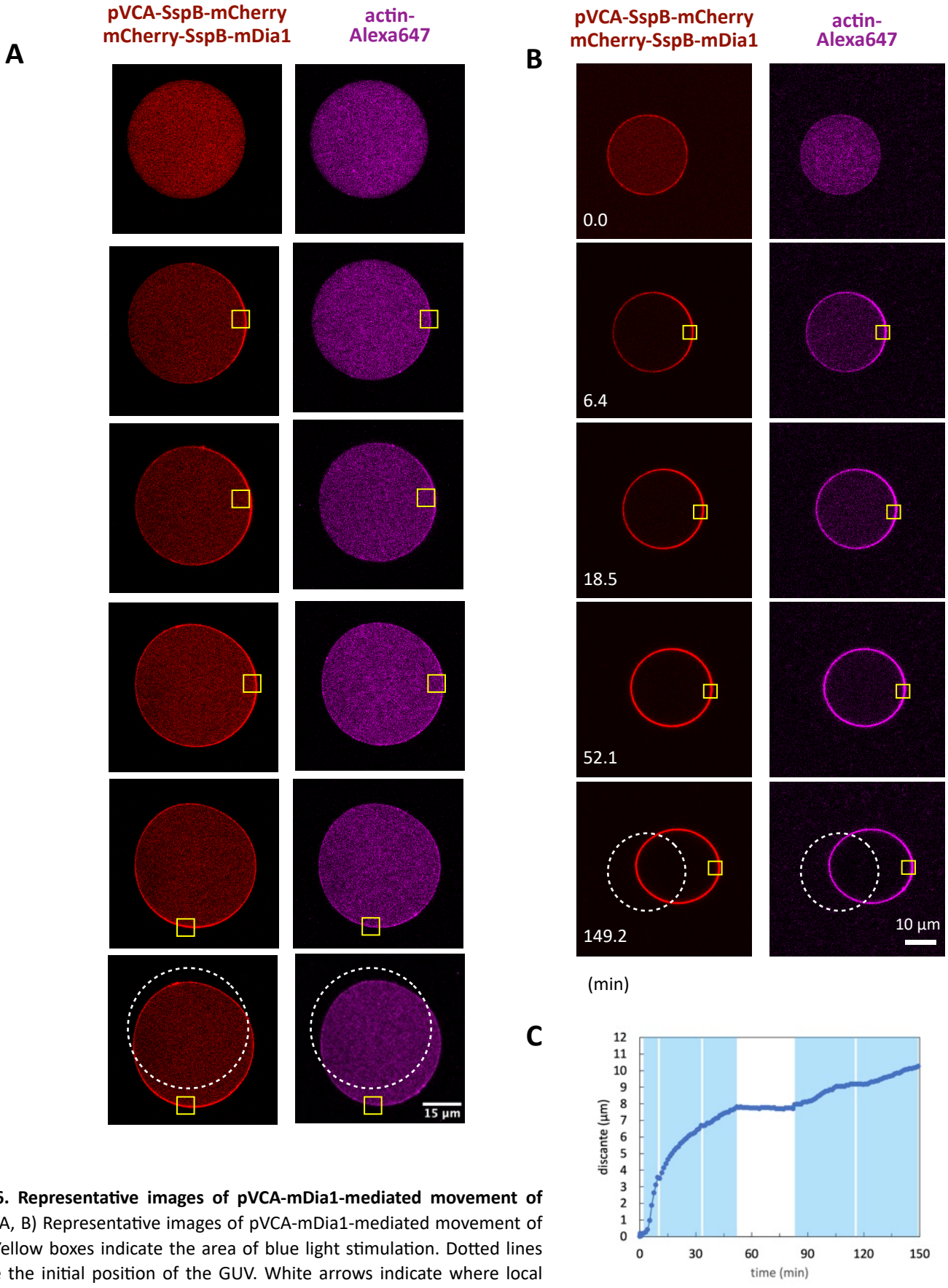

Fig. S16. Representative images of pVCA-mDia1-mediated movement of GUVs. (A, B) Representative images of pVCA-mDia1-mediated movement of GUVs. Yellow boxes indicate the area of blue light stimulation. Dotted lines indicate the initial position of the GUV. White arrows indicate where local protrusions arose. (C) Distance the front side of GUV membrane moved forward. Data was quantified from the images of (B). Blue areas indicate the periods of blue light stimulation.